Dark Matter and Extragalactic Gas Clouds in the NGC 4532 / DDO 137 System

G. Lyle Hoffman

Dept. of Physics, Lafayette College, Easton, PA 18042; hoffmang@nova.phys.lafayette.edu

Nanyao Y. Lu

IPAC, Mail Stop 100-22, California Institute of Technology, Pasadena, CA 91125;
lu@ipac.caltech.edu

E.E. Salpeter

Center for Radiophysics and Space Research, Cornell University, Ithaca, NY 14853;
salpeter@spacenet.tn.cornell.edu

and

Bryan M. Connell

Dept. of Physics, Lafayette College, Easton, PA 18042; connellb@lafayette.edu

ABSTRACT

H I synthesis mapping of NGC 4532 and DDO 137, a pair of Sm galaxies on the edge of the Virgo cluster, is used to determine rotation curves for each of the galaxies and to resolve the structure and kinematics of three extragalactic H I clouds embedded in an extended envelope of diffuse H I discovered in earlier Arecibo studies of the system. The H I masses of the three clouds do not appear to be sufficient for them to be self-gravitating; however, their H I masses and dynamical masses are very similar to those of faint Im galaxies in the Virgo cluster. The peak H I column density of each of the clouds is close to the star formation threshold, but CCD images in B and R reveal no trace of stars or star formation. If the system is gravitationally bound and in Virial equilibrium, we find its total mass to be ten times that within the outermost H I contours of the individual galaxies and clouds. Arecibo mapping finds as much diffuse gas outside the 5 objects as VLA mapping finds inside. One possible way to account for the velocity field and the large quantity of diffuse gas is to assume that DDO 137, the extragalactic clouds and other apparent tidal features are due to gas infall into clumps within the dark matter potential of the group, and that prior to the interaction the group consisted of an irregular galaxy (NGC 4532) and a large, star-poor H I cloud like H I 1225+01 (Giovanelli et al. 1991).

Subject headings: Galaxies: Individual: NGC 4532; Galaxies: Individual: DDO 137; Galaxies: Irregular; Galaxies: Intergalactic Medium; Galaxies: Photometry; Galaxies: Quasars: Absorption Lines; Radio Lines: Galaxies

1. Introduction

Studies of galaxy pairs and small groups in many cases reveal extended streams and detached clouds of H I at considerable distances from the stellar components of the interacting galaxies (e.g., Haynes et al. 1979; Haynes 1981; van Moorsel 1988; van Driel et al. 1992; Chengalur et al. 1994; Li & Seaquist 1994; Yun et al. 1994; Elmegreen et al. 1995b; Hibbard & van Gorkom 1996; Kaufman et al. 1997; Nordgren et al. 1997a,b; earlier references are cited in each of those papers). The streams and clouds are generally assumed to be generated tidally from galaxies that were previously well separated, and dynamical modelling (Toomre & Toomre 1972; Howard et al. 1993; Sofue 1994; Elmegreen et al. 1995a; Dubinski et al. 1996; Mihos & Hernquist 1996; Barnes & Hernquist 1996; Mihos et al. 1998; earlier work is reviewed by Barnes & Hernquist 1992) generally confirms that the tidal assumption is plausible although the simulations do not usually achieve the pronounced distension of the H I relative to the stars that is often seen in the observed cases (however, see Smith et al. 1997).

It has been suggested that some Lyα absorption lines, especially the Lyman Limit Systems (LLS), arise from tidally distended gas around individual galaxies (van Gorkom 1993) or within groups of galaxies (Morris & van den Bergh 1994; Mo & Morris 1994). The H I in interacting systems in any case serves as an historical record allowing the trajectories of the interacting galaxies to be traced back in time in some cases (Phookun et al. 1992; Chengalur et al. 1995; Elmegreen et al. 1995). Condensations of gas within the H I tails appears in some instances to form new dwarf galaxies (Mirabel et al. 1992; Elmegreen et al. 1993; Duc & Mirabel 1994; Hibbard et al. 1994; Hunsberger et al. 1996; Malphrus et al. 1997).

On the other hand, not all diffuse, extended H I clouds appear to have been generated tidally from previously more compact galaxies. Tidal effects may have shaped the Leo ring, but the progenitor does not appear to have been any of the optically identified galaxies in the group (Schneider 1989). The large, diffuse cloud H I 1225+01 (Giovanelli et al. 1991) appears to be well isolated from any galaxy large enough to have exerted tidal influence. In both cases the H I gas appears to have never been part of any optically bright galaxy, and

its dynamics appears to be controlled by dark matter potential wells of galaxy group scale rather than by tides due to individual galaxy halos (see also Hoffman et al. 1998).

NGC 4532 and DDO 137 were initially mapped by us at Arecibo[1] as two distinct irregular galaxies (Helou, Hoffman & Salpeter 1984; Hoffman et al. 1987), but a chance reference beam for an unrelated observation lead to our discovery of a large, diffuse cloud of H I surrounding the pair (Hoffman et al. 1992, 1993). Indications from the Arecibo maps of condensations within the diffuse cloud, but well outside the optical images of the two galaxies, motivated the Very Large Array[2] maps presented here. A desire for finer spatial resolution of the two main galaxies was another motivating factor. CCD imaging was undertaken to see if any low surface brightness optical features could be found in the condensations within the diffuse cloud, and to investigate the star formation histories of the two galaxies. As we shall detail below, we do not think that tides acting on the H I reservoirs of two initially well-separated irregular galaxies can account for the diffuse H I envelope. This system seems to be another example of a primordial, star-poor cloud of H I reacting to a clumpy group-scale dark matter halo.

Optical details culled mainly from de Vaucouleurs et al. (1991, hereafter RC3) are presented in Table 1, which lists for each member galaxy the coordinates (epoch 1950) of the nucleus; the morphological type as coded by Binggeli et al. (1985); the optical heliocentric velocity; our assumed distance, taken to be the same as the Virgo cluster core ; the blue apparent magnitude B_T^0 corrected for inclination and Milky Way extinction, from RC3; the blue absolute magnitude determined from that assumed distance and B_T^0; and the optical diameter at the 25 mag $['']^{-2}$ isophote.

A brief description of the CCD imaging is given in Sect. 2. Details and results of our H I synthesis mapping are given in Sect. 3. In Sect. 4 we discuss the dynamics and possible evolutionary scenarios for the system. We end with a summary and conclusions in Sect. 5.

2. CCD imaging

Both NGC 4532 and DDO 137 were observed in U, B, V, R and I with the Palomar 60-inch telescope equipped with a TK 2048x2048 CCD chip under photometric conditions.

---

[1]The Arecibo Observatory is part of the National Astronomy and Ionosphere Center, which is operated by Cornell University under a management agreement with the National Science Foundation.

[2]The Very Large Array of the National Radio Astronomy Observatory is a facility of the National Science Foundation, operated under cooperative agreement by Associated Universities, Inc.

For NGC 4532, we also obtained an Hα image. These images will be fully described in a later paper where we study the current and past star formation in these galaxies (Lu et al. 1998, hereafter referred to as LHS98). Here, we make use of the B and R images only. With a pixel size of 0.742″, the CCD field is large enough for us to put two of the three H I "clouds" of the system (i.e., Clouds A and B; see Sect. 3.3) on the CCD image of DDO 137 and Cloud C on the image of NGC 4532. The deep R image of DDO 137 has an r.m.s. sensitivity of ~ 26 mag arcsec^{-2}. But at this level, none of the H I clouds is detected optically.

Elliptical contours are fit to each of the galaxy images to extract a surface brightness profile, following the prescription given by Lu et al. (1993). The resulting surface brightness profiles (see Fig. 7 for NGC 4532 and Fig. 12 for DDO 137) are used in this paper to derive some integrated galactic parameters and to constrain the luminous matter in these galaxies. In Table 2, we give for each galaxy its total magnitude in B and the integrated color $B_T - R_T$; the isophotal diameters at B 25 and 26 mag arcsec^{-2}, respectively; and the following B-band parameters for its disk component from an exponential disk fit: the mean ellipticity, the position angle, the exponential scale length r_s as defined in $\mu(r) = \mu_0 + 1.086r/r_s$, and the central surface brightness μ_0. For each parameter, we also give its estimated r.m.s. uncertainty.

3. Neutral hydrogen observations

The H I mapping for these galaxies was conducted at the Very Large Array in two observing sessions as detailed in Table 3, which lists for each source the date of the observing run, the pointing center (epoch 1950), the heliocentric velocity to which the receivers were tuned, the array configuration, the number of spectral channels and channel separation in velocity units, and the time spent on source during the observations, not including time spent on calibrators. We have also listed the resulting beam size in arcsec, the rms noise per channel, and the 3σ detection limit for H I column density in each channel. We obtained both R and L circularly polarized data. We found, however, that we could not eliminate striping of the C or D array maps as long as the R polarization data was retained, so we made maps using L polarization only. On-line Hanning smoothing was employed throughout, and the observations were calibrated using sources from the VLA calibrator list. Calibration and data-editing were accomplished using standard AIPS tasks. Continuum was subtracted in the uv domain using the task UVBAS, and maps were made and CLEANed using IMAGR with robustness parameter 0 for the best compromise between spatial resolution and maximum signal-to-noise. After imaging, each data cube

was corrected for the VLA primary beam.

Following common practise, we have abbreviated the names so that the field "N4532" is centered on the optical image of NGC 4532 while "DDO 137" is centered a few arcmin west of the optical image of DDO 137 in order to give maximum sensitivity to the H I plume extending to the west of the galaxy as seen in our Arecibo mapping (Hoffman et al. 1992, 1993). The field "N4532/D137" is centered in the region between the two galaxies to provide maximum sensitivity to H I condensations within that region of the cloud enveloping the two galaxies.

We obtained data for two fields using the D array, one field centered on NGC 4532 and the second nearly due S, a few arcmin W of the optical image of DDO 137. Since significant emission seems to be confined to the region of overlap in the two D array fields, we combined them as follows: Each uv data set was first shifted to a common tangent point using AIPS task UVFIX; the sets were then combined using task DBCON. IMAGR was run on the combined dataset, producing maps with a $46'' \times 42''$ synthesized beam, 1.6 mJy Bm^{-1} rms, and a 3σ column density limit of 2.8×10^{19} atoms cm^{-2}. Finally, we applied half the primary beam correction for each original pointing center. The result is a data cube that exhibits the same column densities near the centers of each galaxy, but which shows the diffuse emission more clearly than either of the separate fields. We similarly combined the D array and C array datasets, weighting the primary beam corrections by the number of visibilities in each data set. The result is a final set of maps with an $18.5'' \times 16.7''$ synthesized beam and rms noise 0.57 mJy Bm^{-1} per channel, or a 3σ column density limit of 6.4×10^{19} atoms cm^{-2}. The C+D array mosaic is shown in Fig. 1, where we have integrated over consecutive sets of three channels. Earlier attempts to merge the datasets using the maximum entropy method task VTESS produced a large smear of apparently spurious emission across the center of the field; that is why we resorted to the method described above. Efforts at merging both VLA datasets with our single-dish Arecibo map (Hoffman et al. 1993, hereafter HLS+) are underway (Connell 1998), but our thrust here is to consider the VLA and Arecibo data in parallel.

In addition to emission from each of the two optical galaxies, we have clearly detected emission from three clouds distinct from those galaxies (but still embedded within the low column density envelope we found in our Arecibo mapping [HLS+]). We will call these clouds A, B and C as labeled in Fig. 2 where the 0th moment map for the entire region is superimposed on a Digitized Sky Survey[3] image. Cloud B is part of the extended plume

---

[3]The Digitized Sky Surveys were produced at the Space Telescope Science Institute under U.S. Government grant NAG W-2166. The images of these surveys are based on photographic data obtained

stretching W and S from DDO 137 in the Arecibo map (HLS+), which is evident as low level emission in each cube at velocities 1990–2052 km s^{-1}. Weak absorption against a central source in NGC 4532 is evident at velocities $\leq$ 1979 km s^{-1}; the feature is shown integrated over velocity in Fig. 3.

3.1. NGC 4532

The total H I map and velocity field of the SmIII galaxy NGC 4532 are shown in Figs. 4 and 5. The total H I emission, integrated over the D array map, is 33.2 Jy-km s^{-1}, or $2.8 \times 10^9 d_{19}^2$ M$_\odot$, where d_{19} is the distance to the galaxy, assumed to be the same as that to the Virgo cluster, in units of 19 Mpc. For the merged C+D array map, we find 35.2 Jy-km s^{-1}, or $3.0 \times 10^9 d_{19}^2$ M$_\odot$. This is $\sim$ 25% less than the flux we attribute to NGC 4532 in our Arecibo mapping (see Table 4; the fluxes reported in HLS+ did not properly correct for beam overlaps), indicating that we may have resolved out some diffuse flux (or that some flux previously attributed to NGC 4532 is now being attributed to distinct tidal features). The H I distribution is displaced from the optical image of the galaxy in the direction of DDO 137, and there is a flaring of H I toward the E with a distinct tail of H I extending from the S end of the galaxy toward the E. The velocity field is similarly distorted; at the N end the contours are centered on the optical major axis and are consistent with a rising rotation curve symmetric about the optical center. But to the S the contours are skewed, probably by tidal interaction, and the flaring H I toward the E evidently is kinematically distinct from the rest of the H I in the galaxy.

Although the observed velocity field does not constrain the position angle nor inclination of the innermost rings of NGC 4532, we do obtain convergence for the annulus having inner radius 50″ and outer radius 70″. Consequently we adopt those values: position angle of the receding end of the major axis 347°, inclination 72°, systemic velocity 2005 km s^{-1}, for all rings of the galaxy. The systemic velocity was chosen to make the central part of the rotation curve symmetric. The resulting rotation curve is displayed in Fig. 6. It appears to flatten on the approaching (SE) end, but continues to rise in more-or-less solid-body fashion on the receding end of the major axis. However, there are clear signs of extragalactic influence on the H I distribution, and that may have some effect on the velocity field of the outermost gas. The maximum "rotation" speed observed is 111 km s^{-1},

---

on the receding side of the galaxy; the approaching side appears to level off at a velocity of about 63 km s^{-1}. If we average the rotation velocities within entire rings, as shown in Fig. 8 below, the maximum rotation speed is 102 km s^{-1} at a radius of 90.1″ = 8.3 kpc. The second moment map indicates a rather uniform velocity dispersion within the C+D array beam, around 20 km s^{-1} over most of the map, decreasing to 10 km s^{-1} at the outskirts and with one large off-center region in which the dispersion rises above 30 km s^{-1}. The relevant dispersion for dynamical considerations is that in the outer regions; we adopt a value of $\sigma_z = 18$ km s^{-1}, the average over the SE and NW portions of the second moment field. The dynamical mass $M_{dyn} = (v_{rot}^2 + 3\sigma_z^2)r/G$ is then $2.20 \times 10^{10}d_{19}$ M$_\odot$.

The surface brightness profiles in B and R, from LHS98, and the H I surface density profile of NGC 4532 are shown in Fig. 7. Neither the gas mass surface density (including the contribution from primordial helium by multiplying by a factor of 4/3) nor the stellar mass surface density (obtained from the R surface brightness profile, assuming a constant M/L_R) is precisely exponential, but reasonable exponential fits can be made to each surface density distribution and to their sum. In Fig. 8 we show the contributions of those exponential disks to the rotation curve of the galaxy, with M/L_R adjusted to match the inner portion of the star-plus-gas disk to the corresponding portion of the rotation curve (i.e., we adopted the maximum disk hypothesis for the purposes of these figures). $M/L_R = 0.2$M$_\odot$/L$_\odot$ is the largest mass-to-light ratio we can accomodate (and is probably an overestimate; see Bottema [1997]). If the rotation curve averaged within entire annuli of the galaxy is appropriate dynamically, we need a significant contribution from dark matter in the outer parts of the galaxy. If, however, the flat approaching side of the rotation curve is the appropriate one, with the receding side being more severely disturbed by interaction effects, then we do not require any dark matter in this galaxy.

3.2. DDO 137

Corresponding maps of total H I and velocity field for the SmIV galaxy DDO 137, from the merged C+D array data cube, are displayed in Figs. 9 and 10. The integrated emission in the merged D array map is 5.87 Jy-km s^{-1}, or $5.0 \times 10^8 d_{19}^2$ M$_\odot$; for the C+D combination we find 6.82 Jy-km s^{-1}, or $5.8 \times 10^8 d_{19}^2$ M$_\odot$. We cannot compare directly to the Arecibo map in this case, since the Arecibo mapping did not allow us to separate out DDO 137 from the plume extending W and curving S from the galaxy. In contrast to those presented above for NGC 4532, neither the total H I map nor the velocity field show pronounced signs of extragalactic influence. The relatively weak rotation of the galaxy appears approximately solid-body in form over most of the first-moment map.

The position angle from elliptical fits to the isophots of DDO 137 in LHS98 is 127°, but the kinematic major axis is apparently very close to EW. Fitting the velocity field within consecutive annuli, with the inclination held fixed at 43° as determined optically since it is not well constrained by the H I data, indicates that the position angle of consecutive rings gradually shifts from about 92-96° for inner rings to about 80° for the outermost couple. To plot the rotation curve shown in Fig. 11, we held inclination, center position and systemic velocity fixed for all rings, but allowed the position angle to be determined by the fit. The receding (E) side of the galaxy displays a relatively normal rotation curve, rising linearly in the central regions and appearing to flatten for radii beyond 40″. But on the approaching side of the galaxy, the rotation curve appears to be essentially flat from 20″ out, with an apparent rise at the outermost ($> 60″$) rings. There are indications of non-circular motions, however, so the outermost rings should regarded with some suspicion. In particular, the outermost rings may be sampling portions of Cloud B rather than DDO 137 itself. The second moment map gives an average velocity dispersion $\sigma_z = 12$ km s^{-1} within the C+D array beam. If we can take at face value the highest measured rotation speed, 47 km s^{-1}, on the receding side of the galaxy, farthest from the apparent tidal stream toward Cloud B, we find a dynamical mass $M_{dyn} = 4.5 \times 10^9 d_{19}$ M$_\odot$.

The surface brightness profiles in B and R, from LHS98, and the H I surface density profile of DDO 137 are shown in Fig. 12. The gas mass surface density includes the contribution from primordial helium, by multiplying by a factor of 4/3, and the stellar mass surface density is obtained from the R surface brightness profile, assuming a constant M/L_R. As for NGC 4532, reasonable exponential fits can be made to each surface density distribution and to their sum. In Fig. 13 we show the contributions of those exponential disks to the rotation curve of the galaxy, with M/L_R adjusted to match the inner portion of the star-plus-gas disk to the corresponding portion of the rotation curve (i.e., we adopted the maximum disk hypothesis for the purposes of these figures). In this case $M/L_R = 1.8$M$_\odot$/L$_\odot$ gives a reasonable fit to the entire rotation curve, except for the outermost point which is probably affected by non-circular gas motions. That is, however, an exceptionally high value of M/L_R (and is probably an overestimate; see Bottema [1997]); perhaps the agreement in shape is fortuitous.

3.3. Three extragalactic clouds

Cloud A, detected separately in the Arecibo spectra, the D array data and the C array data, is clearly visible in the total H I map about 6′ E of NGC 4532, 7′ due N of DDO 137. The total H I emission from the cloud, summed over the channels that show line emission

at that location, is shown in Fig. 14. It is resolved by our C array data, but is only a few beamwidths across. The velocity field and second moment map are shown in Fig. 15. There is some indication of rotation, with the NW end having lower velocity than the SE end, but the end to end difference is only about two of our velocity channels. Cloud B is a concentration within the extended plume that extends W, then curves S, from DDO 137 in our Arecibo map (HLS+). It is visible as a distinct cloud in the D array and C array data separately. The total H I map is shown in Fig. 16; it is clearly resolved by our C array data. The velocity field and second moment map are shown in Fig. 17. The cloud is not rotating in any regular fashion, although there are larger velocity gradients within Cloud B than within Cloud A. Cloud C (Figs. 18 and 19) appears at lower velocity than any other feature in the maps, primarily in the 1885 and 1896 km s^{-1} channels. It is visible in the Arecibo data as well as in the C and D array data separately.

4.   Discussion

4.1.   Comparisons to Arecibo spectra

Table 4 compares measured quantities from the VLA mapping reported here to corresponding quantities from our Arecibo mapping reported in HLS+. Unfortunately, the integrated H I fluxes and hydrogen masses given in Table 2 of HLS+ for the components of the NGC 4532 / DDO 137 system did not correctly account for beam overlaps; the values cited in Table 4 of this paper supercede those reported earlier. Although the integrated H I fluxes for the VLA data for each of the two main galaxies falls somewhat short of the H I emission integrated over the Arecibo spectra attributed to those galaxies, we find much better agreement with the single Arecibo spectra obtained when the Arecibo telescope was pointed at the optical centers of each galaxy. For NGC 4532, we measured 42.3 Jy-km s^{-1} (Hoffman et al. 1987) at Arecibo, which reduces to 34.7 Jy-km s^{-1} when sidelobe contributions are subtracted out (HLS+). The latter is consistent with the VLA measurement reported above, suggesting that the array measurements have resolved out some structure larger than the 3.3′ Arecibo beam. For DDO 137, the Arecibo measurements were 6.4 Jy-km s^{-1} for the uncorrected single beam (Hoffman et al. 1987) and 8.1 Jy-km s^{-1} for a separate measurement after sidelobe subtraction (HLS+), which was minimal in this case. Evidently the notorious single-beam flux errors, typically assumed to be around 20% in magnitude, are at work in those DDO 137 single-beam measurements. The smaller value is consistent with the integrated VLA flux reported above.

The integrated spectra from the merged D+C array data cube also agree quite well in detail with the single beam Arecibo spectra acquired when Arecibo was pointed at the

optical centers of the two galaxies. Fig. 20 compares the spectra for each of the galaxies. Clearly measurements of systemic velocity and profile widths made from these spectra would agree within a fraction of the VLA channel spacing as shown in Table 4. For NGC 4532, half the Arecibo profile width at 50% of the nearest peak (80.5 km s^{-1}) is a bit smaller than the maximum rotation velocity inferred from the VLA map (102 sin 72° = 97 km s^{-1}). The inferred systemic velocities do not agree quite so well: 2020 km s^{-1} for the Arecibo profile compared to 2005 km s^{-1} for the VLA map. For DDO 137, half the Arecibo profile width at 50% of peak is 33.4 km s^{-1} while the maximum rotation velocity from the VLA map gives 47 sin 43° = 32 km s^{-1}. The systemic velocity taken to be the midpoint of the points where the Arecibo profile falls to 50% of its peak is 2066 km s^{-1}; we inferred a value of 2060 km s^{-1} from the VLA velocity field.

Integrated spectra for each of the three extragalactic clouds are compared to the Arecibo spectra from the closest pointings in Figs. 21, 22 and 23. The integration in each case extends over the largest contiguous contour in Figs. 14, 16 or 18. Here the agreement is not so good, because the Arecibo beam is not pointed at the center of the cloud in each case and has collected flux from other parts of the plume or from the outskirts of the galaxies. In the case of Cloud A, the bump in the Arecibo spectrum extending up to 2100 km s^{-1} is apparently due to incompletely subtracted sidelobes of NGC 4532. For Cloud B, confusion with DDO 137 and the extended plume makes it impossible for us to separate out an H I mass for the cloud alone from Arecibo spectra, but for Clouds A and C we can interpolate among the Arecibo spectrum nearest to each cloud's position and the six nearest neighbor beam positions (with some judgment by eye of what portion of each spectrum to attribute to the cloud). The resulting estimated H I masses, with uncertainties > 20%, are displayed in Table 4.

4.2. Dynamical masses of the extragalactic clouds

The extreme velocities encountered within Cloud A are 1930 and 1955 km s^{-1}, at opposite ends of the cloud separated by about 57″ = 5.2d_{19} kpc. This suggests rotation, but the isovelocity contours are far from regular. The second moment map has an average velocity dispersion $\sigma_z = 6.3$ km s^{-1}. If we assume that the cloud is in simple rotation and that our perspective is edge-on — neither assumption is likely to be true — we have a dynamical mass $M_{dyn} = (v_{rot}^2 + 3\sigma_z^2)r/G = 3.3 \times 10^8 d_{19}$ M$_\odot$. If the cloud is indeed rotating this is likely to be an underestimate of the total mass since any inclination other than the assumed 90° will increase the estimate. The integrated H I amounts to 1.1 Jy km s^{-1}, or $9.0 \times 10^7 d_{19}^2$ M$_\odot$, so the H I mass alone is probably not sufficient to bind the cloud.

For Cloud B, which we take to be the largest distinct clump near the center of Fig. 16, the situation is even less clear. The extreme velocities are approximately 1980 and 2050 $km\,s^{-1}$, but the low velocity occurs in the center of the cloud. It would be incorrect to associate this velocity field with circular rotation. The width of the integrated spectrum, Fig. 22, is 88 $km\,s^{-1}$ at the points 50% down from the peaks of the double-horned profile. The velocity dispersion, from the average over the second moment map, is $\sigma_z = 15$ $km\,s^{-1}$. The linear dimension of the cloud is $104''$, or $9.6d_{19}$ kpc. If we take half the profile width as an indicator for the line-of-sight component of the turbulent velocity v_{turb} within the cloud (incorporating the beam-scale velocity dispersion σ_z), we find a dynamical mass $M_{dyn} = 3v_{turb}^2 r/G = 6.5 \times 10^9 d_{19}$ $M_\odot$. The integrated H I mass is 2.6 Jy-km s^{-1}, or $2.2 \times 10^8 d_{19}^2$ $M_\odot$. If Cloud B is gravitationally bound, evidently much dark matter is required. But the assumption that it is in Virial equilibrium is highly suspect, since the cloud lies in an extended plume.

Cloud C likewise does not have a well-ordered velocity field. Within the cloud itself, velocities range from about 1865 to 1905 km s^{-1}, but in this case it is the high velocities which occur near the center of the cloud. The profile width at 50% of the peak of the spectrum, Fig. 23, is 71 $km\,s^{-1}$. The beam-scale line-of-sight dispersion σ_z is about 12 km s^{-1}, averaged over the second moment map. The linear size of the cloud is $86'' = 7.9d_{19}$ kpc. Taking half the profile width to indicate turbulent velocity as for Cloud B, above, we obtain an estimate of the dynamical mass $M_{dyn} = 3v_{turb}^2 r/G = 3.5 \times 10^9 d_{19}$ $M_\odot$. The integrated H I mass is 2.1 Jy-km s^{-1}, or $1.8 \times 10^8 d_{19}^2$ $M_\odot$. The dark matter requirements are not so extreme as for Cloud B, if Cloud C is to be bound, but again the assumption of Virial equilibrium is suspect since Cloud C also lies within an extended stream.

The H I masses and dynamical masses estimated above for all three clouds are very much consistent with those quantities for the faintest Im galaxies in Virgo for which we have H I detections (Hoffman et al. 1987).

4.3. Interaction scenarios and group mass estimates

At a cursory glance, neither the H I distribution of NGC 4532 shown in Fig. 4 nor that of DDO 137 shown in Fig. 9, taken in isolation, alerts the viewer to the complex interactions within the system. Only upon much closer inspection does one notice the asymmetry of the H I around NGC 4532, with a more rapid decrease in column density toward the N than to the S; the flare to the E does not reveal itself until one inspects the individual channel maps (Fig. 1) or the velocity field (Fig. 5). Another possible explanation for the asymmetrical H I distribution around NGC 4532 might be ram pressure by the Virgo cluster intracluster

medium (Phookun & Mundy 1995). However, the galaxy is not close to any X-ray emitting portion of the cluster complex, nor to any particularly dense subcluster. Furthermore, the absorption seen against a continuum source toward the N end of the optical image is a clue that some unusual starburst is going on (LHS98). It seems more likely that the disturbance is caused somehow by interactions within the NGC 4532 / DDO 137 system. Ram pressure against diffuse H I within the system is a possibility, but the well-separated extragalactic clouds and strange kinematics of the diffuse gas lead us to the more likely possibility that a clumpy dark matter halo enveloping the entire system is driving the motions and concentration of the gas. Neither the column density map (Fig. 9) nor the velocity field (Fig. 10) of DDO 137 is unusual for an irregular galaxy; it is only in the larger context of a map showing DDO 137 and Cloud B along with the plume curving to the SW that one realizes that the slight linear extension toward the NW of DDO 137 may in fact be a stream. There is, however, no hint of a stellar tidal stream emanating from either galaxy in the B- or R-band CCD images from LHS98, shown in Fig. 4 and 9.

Could another galaxy be involved? There is no other catalogued galaxy with known redshift within $34'$. The nearest large galaxy is NGC 4570, an $S0_1(7)/E7$, $B_T = 11.84$, galaxy at $62'$ (more than 5 times the separation of DDO 137 from NGC 4532) and $V_\odot = 1730$ km s^{-1} (RC3). On the Digitized Sky Survey it appears to be a classic edge-on S0 with no hint of tidal interaction.

We see no hint of starlight at our R sensitivity limit of 26 mag $['']^{-2}$ at the positions of the clouds in any of the other CCD images (LHS98); the B-band images are shown in Figs. 14, 16 and 18, above. Are these clouds nascent dwarf galaxies, eventually to form stars as in the tidal streams studied by Mirabel et al. (1992), Elmegreen et al. (1993), Duc & Mirabel (1994), Hibbard et al. (1994), Hunsberger et al. (1996), and Malphrus et al. (1997)? The H I masses reported in the preceding section are appropriate to observed dwarf star-forming galaxies (Salpeter & Hoffman 1996; Roberts & Haynes 1994), but the H I mass alone does not appear to be sufficient to gravitationally bind any of the three clouds if they are currently in Virial equilibrium. Dwarf galaxies formed from tidal debris are not expected to have significant dark matter halos (Barnes & Hernquist 1992b; Elmegreen et al. 1993). The central column densities are $5 - 6 \times 10^{20}$ atoms cm^{-2} for each, close to the critical column density for star formation (Kennicutt 1989), but our surface brightness limits are close to the central surface brightnesses of the most extreme low surface brightness (LSB) galaxies known (O'Neil et al. 1997), and more than 2 mag$['']^{-2}$ fainter than most LSB galaxies.

We can estimate the mass of the group of 5 objects (2 galaxies and 3 clouds) on the assumption that the system is in Virial equilibrium either by taking each of the five as a point object tracer of the gravitational potential of the group, using a standard Virial

estimator (e.g., Binney & Tremaine 1987) or by measuring the velocity width of the global H I profile. Both approaches give consistent results: a group mass in the range $3 - 6 \times 10^{11}\,M_\odot$ (see Table 5). This is approximately an order of magnitude larger than the sum of the dynamical masses of all the components, estimated from their rotation curves or H I profile widths. Table 5 also reports the total stellar mass of each luminous component, calculated from the R magnitude with RC3 corrections for internal and Galactic extinction, using the maximum disk M/L_R. The gas mass of each distinct component is also tabulated; it is calculated from the H I mass (VLA measurement for each galaxy or cloud, Arecibo measurement for the system as a whole) by multiplying by a factor of 4/3 to account for primordial Helium gas. We have ignored any contribution from molecular gas.

On a similar vein, the total H I mass of the group as measured at Arecibo is larger by a factor of 2 than the H I masses of the 5 components as measured by the VLA. The extra H I is partly in extended, diffuse clouds that can be associated with each of the two galaxies, but which have been resolved out of the VLA map; but about one-third of the gas lies well outside both galaxies. Furthermore, as we noted in Hoffman et al. (1993), all the supposedly tidal features — all three condensations, Clouds A, B and C, along with the plume stretching out from DDO 137 and the diffuse material extending both E and W from NGC 4532, visible in the Arecibo map but only hinted at in the VLA maps presented here — fall at lower velocities than the two galaxies even though those extragalactic features are spread out in divers directions from each galaxy.

We are led to speculate that these features are not the result of tidal interaction between two Sm galaxies, but rather the interaction between one large Sm galaxy (NGC 4532) and a large H I cloud resembling H I 1225+01 (Giovanelli et al. 1991), each with a large complement of dark matter (or perhaps in a common halo of dark matter). The dark matter haloes are now overlapping, with the more diffuse H I cloud having been disrupted in the process; star formation has proceeded only in the most dense clump (DDO 137) of the fragmented cloud. A star formation history analysis of CCD imaging in UBVRI and Hα is underway (LHS98). Clouds A, B and C may either be manifestations of the tidal interaction between the original H I cloud and the clumpy dark matter potential, or the result of gas falling into dense clumps of dark matter within the common halo. High resolution simulations show that such clumps can survive for significant times within group-scale halos, if their internal densities are sufficiently high (Klypin et al. 1997; Tormen et al. 1997a, b; Ghigna et al. 1998).

4.4. Implications for Ly-α absorption systems

Presumably, if HST spectra were obtained for any QSOs lying behind the extended H I cloud they would exhibit Lyman Limit Systems (LLS). Such absorption systems account for a few percent of the low redshift Ly-α absorptions observed with HST (Storrie-Lombardi et al. 1994; Stengler-Larrea et al. 1995; Bahcall et al. 1996); whereas low redshift Ly-α forest systems are found in galaxy groups with a covering factor near unity (Le Brun et al. 1996; Bowen et al. 1996; Morris et al. 1993), LLS are found much more rarely. We can imagine four scenarios in which a LLS might be found: when the line-of-sight to the QSO (1) falls within the outermost extensions of a galaxy disk but still within the photo-ionization truncation radius, typically a few kpc (Salpeter & Hoffman 1996); (2) falls within the mainly neutral part of a tidal tail (Haynes et al. 1979; van Gorkom 1993); (3) passes through a high velocity cloud (HVC) as in the model of Blitz et al. (1997); or (4) when the line-of-sight passes through a system such as NGC 4532 / DDO 137.

If scenario (1) were the only one possible, LLS would be seen in far less than a few percent of galaxy groups since the area within the few kpc radius out to which neutral hydrogen emission can be traced is a much smaller fraction of a typical loose galaxy group. We do not have firm statistics on the number of groups in which tidal tails can be seen in H I emission, but the number fraction of groups is certainly significant (see reference list given in the Introduction). We also do not have a detailed analysis of what fraction of the area of individual groups is covered by the tidal tails when they are observed; typically only a fraction of each group falls within the synthesis array primary beam or within the pattern of single beams used to map the tidal tail. The same is true for group-wide HVC. So it remains conceivable, but unproven, that scenarios (2) and (3) could account for most LLS. For scenario (4) to account for a significant number of LLS, systems like NGC 4532 / DDO 137, H I 1225+01 (Giovanelli et al. 1991) and the Leo Ring (Schneider 1989) would have to comprise a few percent of all galaxy groups. All three were discovered by chance reference beams from unrelated observations; very few groups have been mapped to sufficiently large distances from individual member galaxies and with sufficient sensitivity to rule out the presence of diffuse emission at column density around 2×10^{19} atoms cm^{-2}. The Arecibo H I Strip Survey (Zwaan et al. 1997) shows that star-poor gas clouds are not common in the general field, but does not place strong constraints on the number of groups which harbor such systems. One might argue that the density of gas in such a cloud, normally below the photo-ionization threshold when the cloud is in the general field, rises above that threshold when the cloud is concentrated within the deeper gravitational potential well of a group.

5. Summary

Neutral hydrogen synthesis array mapping of the extended gas cloud around the widely separated galaxy pair NGC 4532 / DDO 137 reveals three H I clouds well separated from the two main galaxies. The H I masses nad estimated dynamical masses are consistent with those of faint Im galaxies in the Virgo cluster (Hoffman et al. 1987). No stars are visible within these clouds on the CCD images of Lu (1998). The inferred dynamical mass of each cloud, assuming Virial equilibrium, exceeds the H I mass by factors of 3-30. The central column density of each cloud is close to the critical column density for star formation (Kennicutt 1989), but our upper limits on surface brightness are comparable to the central surface brightnesses of the most extreme low surface brightness galaxies known (O'Neil et al. 1997).

The H I distribution and rotation curve of NGC 4532 display some peculiarities consistent with tidal interaction; those of DDO 137 are more nearly in accord with expectations for a low mass irregular galaxy. A maximum disk hypothesis applied to fitting exponential star+gas disks to the observed rotation curves would require very different mass-to-light ratios for the stars in NGC 4532 and those in DDO 137, perhaps consistent with their very different apparent star formation activities (Lu et al. 1998). The shapes of the rotation curves of DDO 137 and of the approaching side of NGC 4532 are consistent with a constant ratio of dark matter to star+gas density at all observed radii in each; however, if the receding side of NGC 4532 is the one less severely afflicted with non-circular velocities (as suggested by all other indications of tidal interaction in the galaxy), then the usual dark matter halo is required.

All available estimators of the total mass of the group (consisting of two galaxies plus three extragalactic clouds) give a total mass an order of magnitude larger than the sum of the masses of the individual objects out to the largest radii measured in the VLA maps, as estimated from their rotation curves or Virial analyses. The H I fluxes reported in Hoffman et al. (1993) were not properly corrected for beam overlaps; we give the corrected fluxes in Table 4. After correction, the total flux at Arecibo still exceeds the sum of all H I masses measured in the VLA mapping by a factor of 2. These facts, along with the kinematic peculiarities of the system, lead us to advance the hypothesis that the system progenitor was a bound pair consisting of the large Sm galaxy NGC 4532 and a large star-poor gas cloud similar to H I 1225+01, each dominated by dark matter. The dark matter halos have now merged, and gas is being accreted into the densest clumps within the common dark matter halo. Star formation has proceeded only in the two densest clumps — NGC,4532, which probably had stars prior to the merger, and DDO,137, which perhaps had no prior stars. Detailed star formation history analysis to follow (Lu et al. 1998) should help us to

constrain this scenario further.

REFERENCES

Bahcall, J.N., et al. 1996, ApJ, 457, 19

Barnes, J.E., & Hernquist, L. 1992a, ARA&A, 30, 705

Barnes, J.E., & Hernquist, L. 1992b, Nature, 360, 715

Barnes, J.E., & Hernquist, L. 1996, ApJ, 471, 115

Binggeli, B., Sandage, A., & Tammann, G.A. 1985, AJ, 90, 1681

Binney, J., & Tremaine, S. 1987, Galactic Dynamics (Princeton: Princeton University Press), 610

Blitz, L., Spergel, D.N., Teuben, P.J., Hartmann, L., & Burton, W.B. 1997, BAAS, 28, 1349

Bottema, R. 1997, A&A, 328, 517

Bowen, D.V., Blades, J.C., & Pettini, M. 1996, ApJ, 464, 141

Chengalur, J.N., Salpeter, E.E., & Terzian, Y. 1994, AJ, 107, 1984

Chengalur, J.N., Salpeter, E.E., & Terzian, Y. 1995, AJ, 110, 167

Connell, B. 1998, Lafayette College Honors Thesis, in preparation

de Vaucouleurs, G., de Vaucouleurs, A., Corwin, H.G., Buta, R.J., Paturel, G., & Fouqué, P. 1991, Third Reference Catalog of Bright Galaxies, (New York: Springer-Verlag) (RC3)

Dubinski, J., Mihos, J.C., & Hernquist, L. 1996, ApJ, 462, 576

Duc, P.-A., & Mirabel, I.F. 1994, A&A, 289, 83

Elmegreen, B.G., Kaufman, M., & Thomasson, M. 1993, ApJ, 412, 90

Elmegreen, B.G., Sundin, M., Kaufman, M., Brinks, E., & Elmegreen, D.M. 1995a, ApJ, 453, 139

Elmegreen, D.M., Kaufman, M., Brinks, E., Elmegreen, B.G., & Sundin, M. 1995b, ApJ, 453, 100

Elmegreen, D.M., Sundin, M., Elmegreen, B.G., & Sundelius, B. 1991, A&A, 244, 52

Ghigna, S., Moore, B., Governato, F., Lake, G., Quinn, T., & Stadel, J. 1998, MNRAS, in press (astro-ph/9801192)

Giovanelli, R., Williams, J.P., & Haynes, M.P. 1991, AJ, 101, 1242

Haynes, M.P. 1981, AJ, 86, 1126

Haynes, M.P., Giovanelli, R., & Roberts, M.S. 1979, ApJ, 229, 83

Helou, G., Hoffman, G.L., & Salpeter, E.E. 1984, ApJS, 55, 433

Hibbard, J.E., Guhathakurta, P., van Gorkom, J.H., & Schweizer, F. 1994, AJ, 107, 67

Hibbard, J.E., & van Gorkom, J.H. 1996, AJ, 111, 655

Hoffman, G.L., Helou, G., Salpeter, E.E., Glosson, J., & Sandage, A. 1987, ApJS, 63, 247

Hoffman, G.L., Lu, N.Y., Salpeter, E.E., Connell, B.M., & Fromhold-Treu, R. 1998, ApJ, in press

Hoffman, G.L., Lu, N.Y., Salpeter, E.E., Farhat, B., Lamphier, C., & Roos, T. 1993, AJ, 106, 39 (HLS+)

Hoffman, G.L., Salpeter, E.E., Lamphier, C., & Roos, T. 1992, ApJ, 388, L5

Howard, S., Keel, W.C., Byrd, G., & Burkey, J. 1993, ApJ, 417, 502

Hunsberger, S.D., Charlton, J.C., & Zaritsky, D. 1996, ApJ, 462, 50

Kaufman, M., Brinks, E., Elmegreen, D.M., Thomasson, M., Elmegreen, B.G., Struck, C., & Klarić, M. 1997, AJ, 114, 2323

Kennicutt, 1989, ApJ, 344, 685

Klypin, A., Gottlöber, S., Kravtsov, A.V., & Khokhlov, A.M. 1997, submitted to ApJ, astro-ph/9708191

Le Brun, V., Bergeron, J., & Boissé, P. 1996, A&A, 306, 691

Li, J.G., & Seaquist, E.R. 1994, AJ, 107, 1953

Lu, N.Y., Hoffman, G.L., & Salpeter, E.E. 1998, in preparation (LHS98)

Lu, N.Y., Hoffman, G.L., Groff, T., Roos, T., & Lamphier, C. 1993, ApJS, 88, 383

Malphrus, B.K., Simpson, C.E., Gottesman, S.T., & Hawarden, T.G. 1997, AJ, 114, 1427

Mihos, J.C., Dubinski, J., & Hernquist, L. 1998, ApJ, in press

Mihos, J.C., & Hernquist, L. 1996, ApJ, 464, 641

Mirabel, I.F., Dottori, H., & Lutz, D. 1992, A&A, 256, L19

Mo, H.J., & Morris, S.L. 1994, MNRAS, 269, 52

Morris, S.L., & van den Bergh, S. 1994, ApJ, 427, 696

Morris, S.L., Weymann, R.J., Dressler, A., McCarthy, P.J., Smith, B.A., Terrile, R.J., Giovanelli, R., & Irwin, M. 1993, ApJ, 419, 524-

Nordgren, T.E., Chengalur, J.N., Salpeter, E.E., & Terzian, Y. 1997a, AJ, 114, 77

Nordgren, T.E., Chengalur, J.N., Salpeter, E.E., & Terzian, Y. 1997b, AJ, 114, 913

O'Neil, K., Bothun, G.D., & Cornell, M.E. 1997, AJ, 113, 1212

Phookun, B., & Mundy, L.G. 1995, ApJ, 453, 154

Phookun, B., Mundy, L.G., Teuben, P.J., & Wainscoat, R.J. 1992, ApJ, 400, 516

Roberts, M.S., & Haynes, M.P. 1994, ARA&A, 32, 115

Salpeter, E.E., & Hoffman, G.L. 1996, ApJ, 465, 595

Schneider, S.E. 1989, ApJ, 343, 94

Smith, B.J., Struck, C., & Pogge, R.W. 1997, ApJ, 483, 754

Sofue, Y. 1994, ApJ, 423, 207

Stengler-Larrea, E.A., et al. 1995, ApJ, 444, 64

Storrie-Lombardi, L.J., McMahon, R.G., Irwin, M.J., & Hazard, C. 1994, ApJ, 427, L13

Toomre, A., & Toomre, J. 1972, ApJ, 178, 623

Tormen, G., Bouchet, F.R., & White, S.D.M. 1997a, MNRAS, 286, 865

Tormen, G., Diaferio, A., & Syer, D. 1997b, submitted to MNRAS, astro-ph/9712222

van Driel, W., Augarde, R., Bottenelli, L., Gouguenheim, L., Hamabe, M., Maehara, H., Baan, W.A., Goudfrooij, P., & Groenewegen, M.A.T. 1992, A&A, 259, 71

van Gorkom, J. 1993, in The Environment and Evolution of Galaxies, ed. J.M Shull & H.A. Thronson (Dordrecht: Kluwer), 345

van Moorsel, G.A. 1988, A&A, 202, 59

Yun, M.S., Ho, P.T.P., & Lo, K.Y. 1994, Nature, 372, 530

Zwaan, M.A., Briggs, F.H., Sprayberry, D., & Sorar, E. 1997, ApJ, 490, 173

TABLE 1. Optical Details

Galaxy	R.A. hhmmss.s	Dec. ddmmss	Type	$V_\odot$ km s^{-1}	Distance Mpc	B_T^0 mag	M_B mag	D_{25} kpc
NGC 4532	123146.8	064443	SmIII	2154	19	11.94	−19.45	15.6
DDO 137	123212.1	063441	SmIV		19	14.58	−16.81	7.1

TABLE 2. CCD Photometry

	N4532	DDO 137
B_T (mag)	12.15 ± 0.02	14.76 ± 0.04
$(B - R)_T$ (mag)	0.71 ± 0.05	0.95 ± 0.07
D_{25} (B) (')	3.03 ± 0.10	1.25 ± 0.07
D_{26} (B) (')	3.53 ± 0.11	1.78 ± 0.11
Ellipticity	0.648 ± 0.07	0.235 ± 0.03
PA ($^\circ$)	159 ± 2	144 ± 13
μ_o (B) (mag $['']^{-2}$)	18.92 ± 0.14	22.81 ± 0.15
r_s (B) ($''$)	16.23 ± 0.52	17.16 ± 1.02

TABLE 3. Very Large Array Observations

	N4532	DDO 137	N4532/D137
Date	29 AUG 92	29 AUG 92	08 DEC 94
R.A. (hhmmss.s)	123146.8	123152.0	123159.6
Dec. (ddmmss)	064443	063200	063942
$V_\odot$ (km s^{-1})	2000	2000	2000
Array	D	D	C
No. of channels	63	63	63
Channel separation (km s^{-1})	10.4	10.4	10.4
Time on source (min)	281	278	322
Beam (arcsec)	51×45	49×46	15×14
rms (mJy/Beam)	2.3	2.1	0.73
3σ limit (10^{19} atoms cm^{-2})	3.5	3.2	11.4

TABLE 4. Comparison of Results

Galaxy (1)	M_{HI}[a] VLA (2)	M_{HI}[b] AO (3)	V_{sys}[c] VLA (4)	V_{sys}[c] AO (5)	ΔV_{50}[d] VLA (6)	ΔV_{50}[d] AO (7)	α_{HI}[e] VLA (8)	D_{HI}[f] AO (9)
NGC 4532	30	39	2005	2024	161	191	5.8	66
DDO 137	5.8	16	2060	2044	64	124	3.4	94
Cloud A	0.9	1.1	1941	1948	34	39	$\cdots$	$\cdots$
Cloud B	2.2	$\cdots$	2022	2020	88	87	$\cdots$	$\cdots$
Cloud C	1.8	3.0	1886	1879	71	82	$\cdots$	$\cdots$
Group	41	83	2003	$\cdots$	$\cdots$	$\cdots$	$\cdots$	149

[a]H I mass in units of $10^8 d_{19}^2$ M$_\odot$

[b]Same units as col. 1; these values supercede those in HLS+

[c]Systemic velocities in units of km s^{-1}

[d]Profile widths at 50%, in km s^{-1}

[e]H I scalelength in kpc

[f]H I maximum diameter in kpc

TABLE 5. Dynamical Masses

Galaxy (1)	v_{rot} km s^{-1} (2)	σ_z km s^{-1} (3)	r d_{19} kpc (4)	M_{dyn} $10^8\, d_{19}\,$M$_\odot$ (5)	$M_\star$ $10^8\, d_{19}\,$M$_\odot$ (6)	M_{gas} $10^8\, d_{19}\,$M$_\odot$ (7)
NGC 4532	102	18	8.3	220	20	40
DDO 137	47	12	7.4	45	15	7.7
Cloud A	12	6	2.6	3.3	$\cdots$	1.2
Cloud B	$\cdots$	44	4.8	65	$\cdots$	2.9
Cloud C	$\cdots$	36	4.0	35	$\cdots$	2.4
Group (20% width)	$\cdots$	141	74	2500	35	111
Group (Virial)	$\cdots$	$\cdots$	$\cdots$	4300	35	111

Fig. 1.— Mosaic of 3-channel integrated contour maps for the merged C and D array datasets of the galaxy pair NGC 4532 / DDO 137. The beam is shown in the lower right corner of the top left pane. Each pane consists of the integral over three channels of the data cube; the velocities of the middle channel in each pane, starting at the upper left and proceeding left-to-right in consecutive rows, are 2136, 2104, 2073, 2042, 2010, 1979, 1948, 1916, 1885, 1854, 1823 and 1791 km s^{-1}. Contours are drawn at -1.6, 1.6, 2.4, 3.6, 5.4, 8.2, 12.3, 18.4 and 27.6×10^{20} atoms cm^{-2}.

DECLINATION (B1950)

12 32 30   15   0031 45   30
RIGHT ASCENSION (B1950)

12 32 30   15   0031 45   30
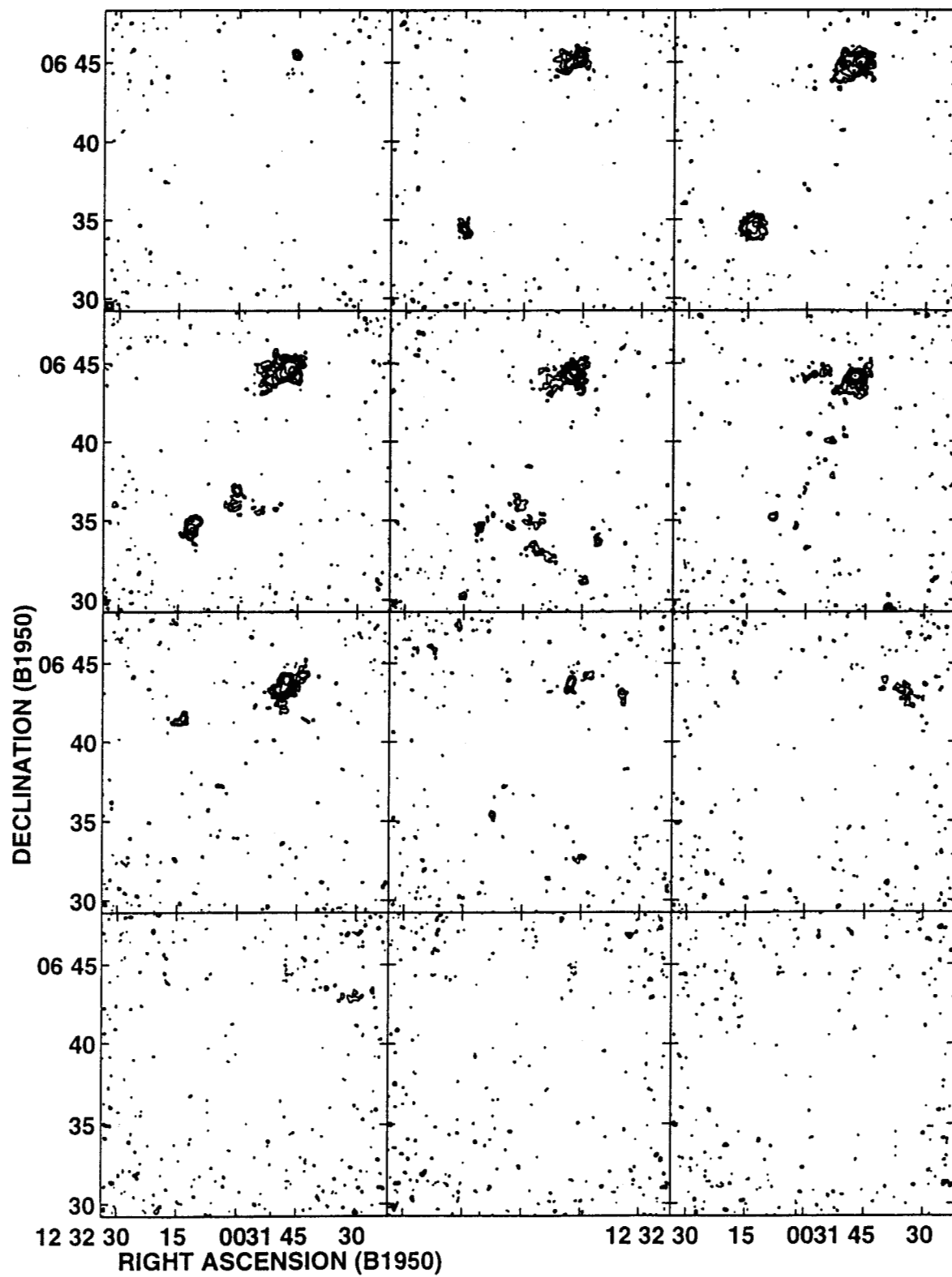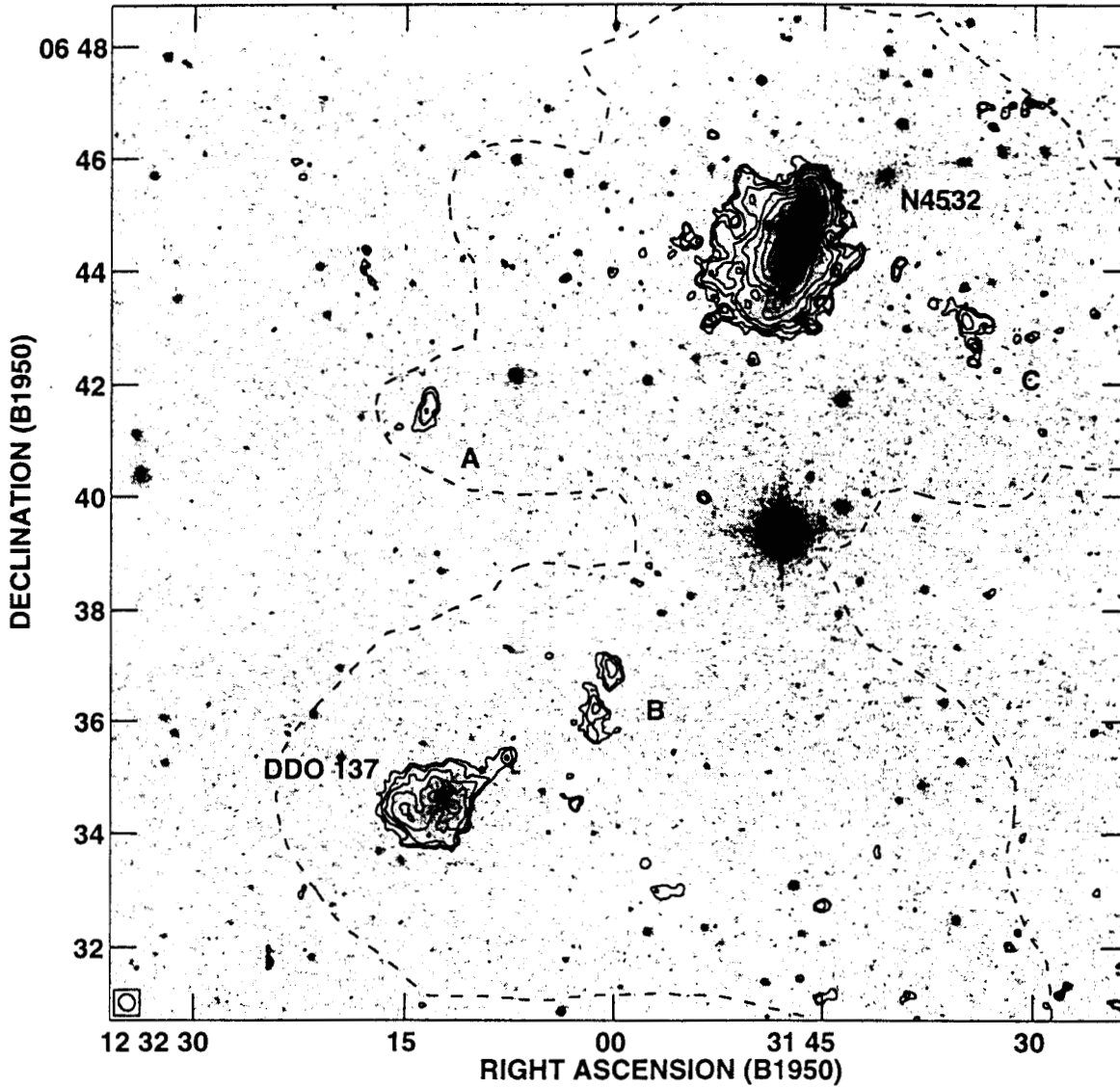
Fig. 2.— Contours of total hydrogen emission from the area around NGC 4532 and DDO 137, integrated over all line-bearing channels for the C+D array combination and superimposed on a greyscale image from DSS. Contour levels from the VLA mapping (*solid line*) are 2.5, 3.8, 5.6, 8.5, 12.7, 19.1, 28.6, 42.9 and 64.3×10^{20} atoms cm^{-2}. The dashed curve shows the outermost contour level from the Arecibo map, at 2.0×10^{19} atoms cm^{-2}. Three detached clouds are indicated.
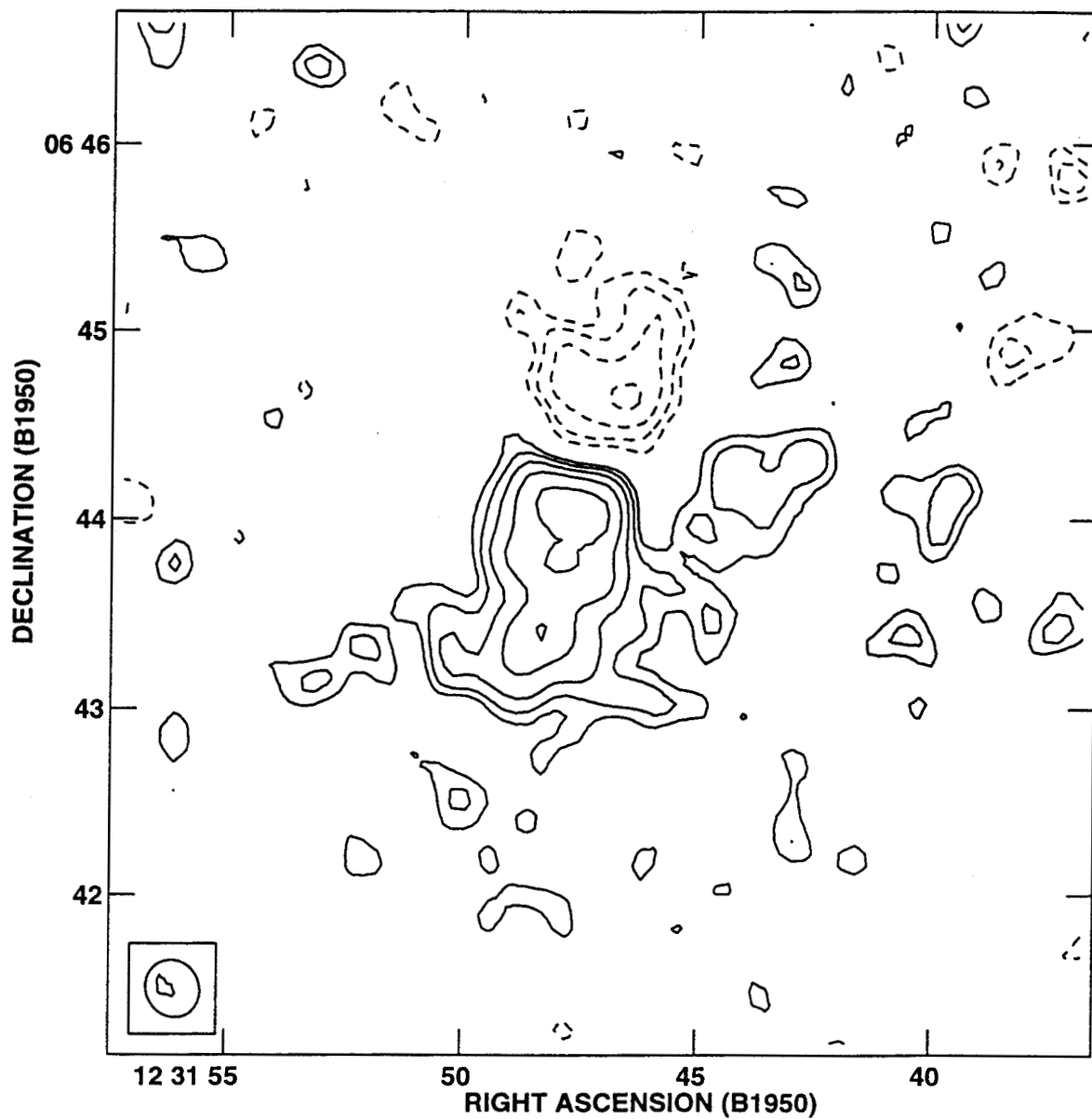
Fig. 3.— Absorption feature at the center of NGC 4532, integrated over velocity for the channels in which it appears in the combined C+D array data cube. The emission in those channels (excluding all channels where no absorption is seen) is shown with solid contours, absorption with dashed contours. The contour levels are -0.40, -0.27, -0.18, -0.12, 0.12, 0.18, 0.27, 0.40 and 0.60 Jy Bm^{-1} km s^{-1}.
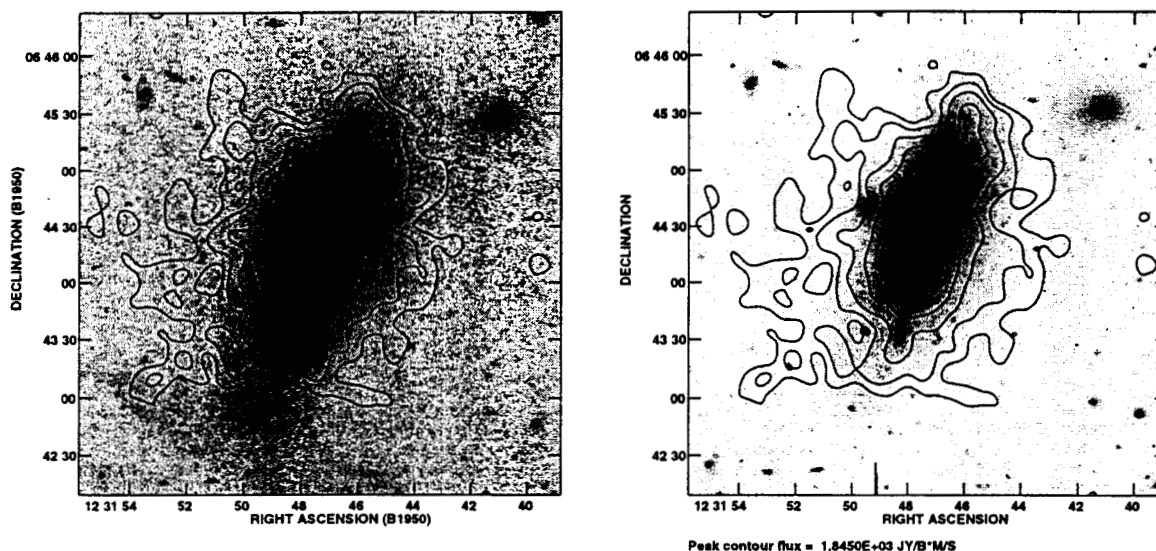
Fig. 4.— Contours of total hydrogen emission from NGC 4532, integrated over all line-bearing channels from our combined C+D cube superimposed on B-band (*left*) and R-band (*right*) CCD images from Lu et al. (1998). The B-band image shows a faint "paper-clip" artifact at the lower left; the cause of the artifact is not well understood, but it is not due to anything related to NGC 4532. Neutral hydrogen contour levels are 8.6, 12.9, 19.4, 29.0, 43.6 and 65.3×10^{20} atoms cm^{-2} for both. The stretch for the B-band image was chosen to reveal the faintest possible features; that for the R-band image is chosen to show more detail of the central part of the galaxy.
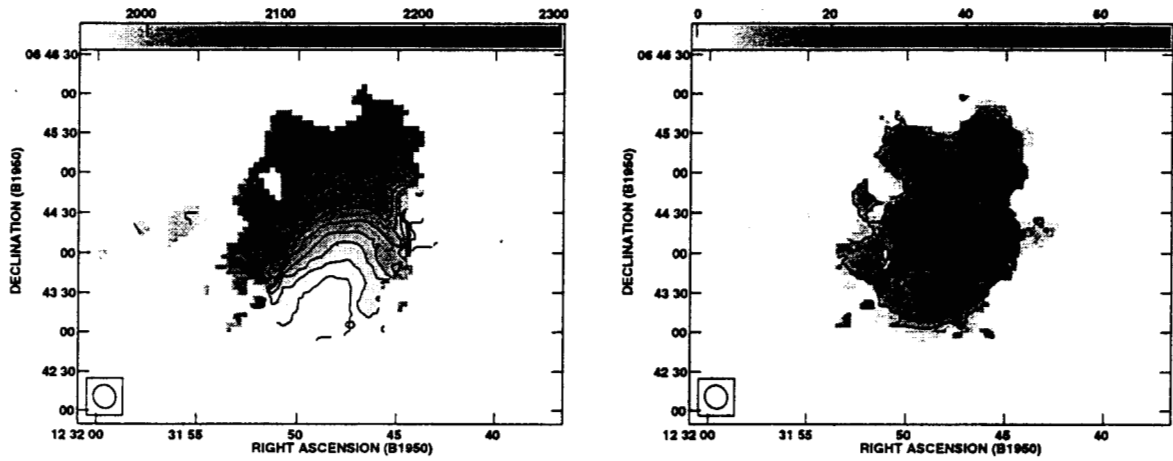
Fig. 5.— Isovelocity contours superimposed on a greyscale image of the velocity field from the merged C+D data (*left* panel) and second moment map (*right* panel) of NGC 4532. Contours are drawn from from 1955 to 2090 in steps of 15 km s^{-1} in the left-hand panel, and from 10 to 40 in steps of 10 km s^{-1} in the right-hand panel.
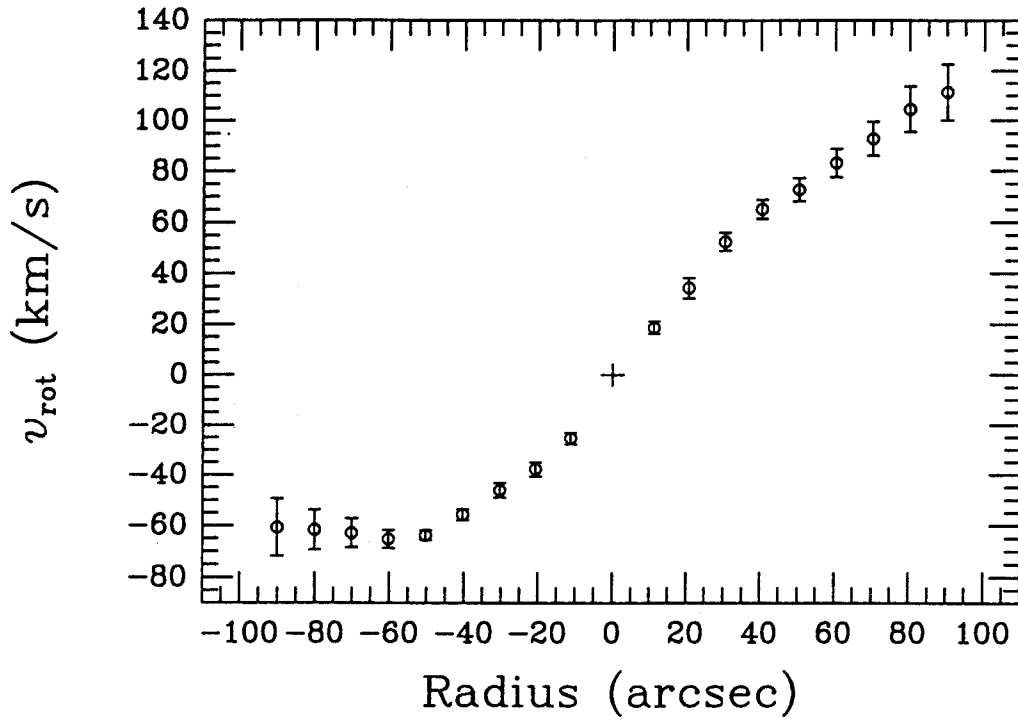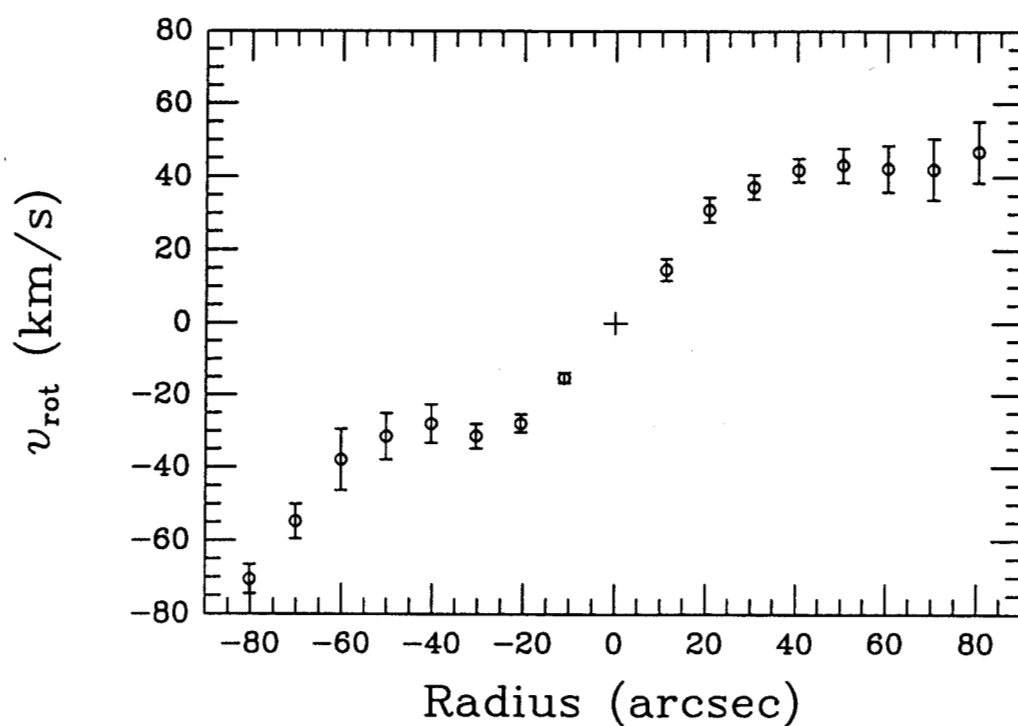
Fig. 6.— Rotation curve for NGC 4532, determined by fitting the velocity field within consecutive annuli. The center position, systemic velocity (2005 km s^{-1}), position angle and inclination were held fixed for all rings at values discussed in the text. Positive velocities are receding and positive radii are toward the NW. The cross marks the center in position and rotation velocity.
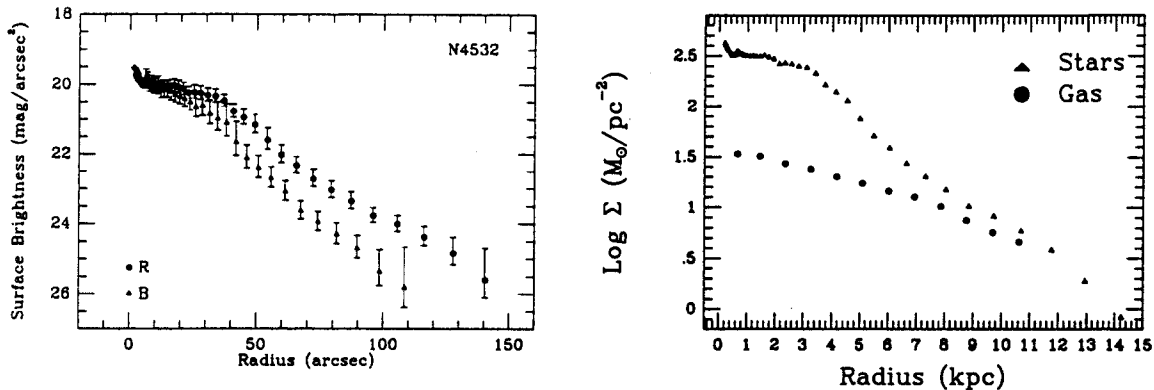
Fig. 7.— (*left panel*) B (*triangles*) and R (*circles*) surface brightness profiles for NGC 4532 from Palomar CCD imaging. (*right panel*) Mass surface densities in stars (*triangles*) and gas (*circles*). We have assumed $M/L_R = 1 M_\odot/L_\odot$ for the purposes of this plot, and have included neutral hydrogen and primordial helium gas but have neglected molecular and ionized gas.
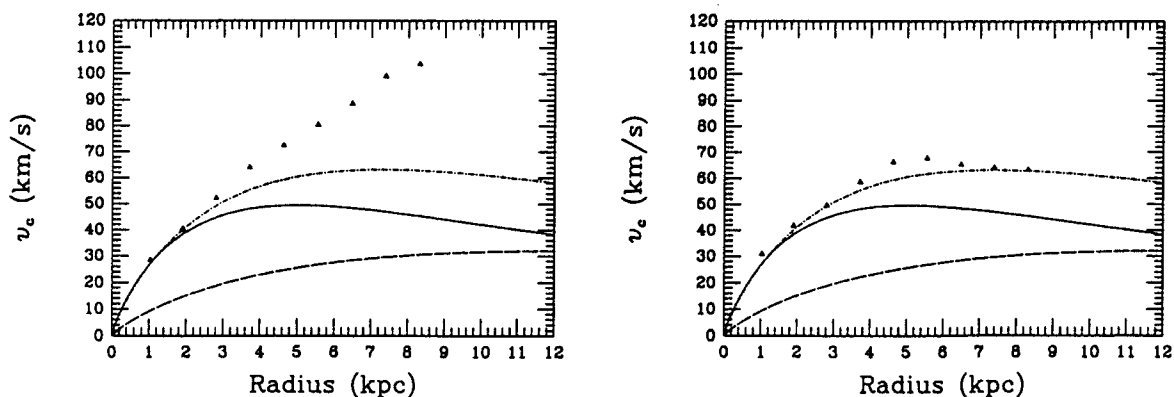
Fig. 8.— The rotation curve of NGC 4532 (*points*) averaged over entire rings (*left panel*) and over the approaching side only (*right panel*), with curves showing the contributions of exponential disks fitted to the stars assuming $M/L_R = 0.2 M_\odot/L_\odot$ (*dotted*), to the gas, including neutral hydrogen and primordial helium (*dashed*), and to the sum of stars plus gas (*dash-dot*). This choice of mass-to-light ratio is close to the maximum disk value.
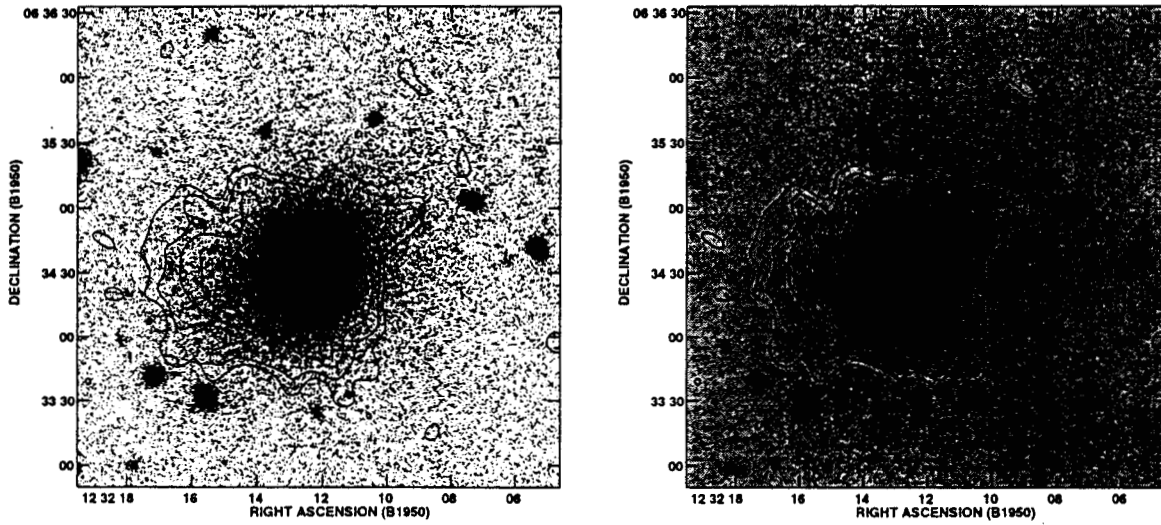
Fig. 9.— Contours of total hydrogen emission from DDO 137, integrated over all line-bearing channels from our C+D array data cube, superimposed on B-band (*left*) and R-band (*right*) CCD images from Lu e al. (1998). Contour levels are −3.2, 3.2, 4.8, 7.3 and 10.9×10^{20} atoms cm^{-2}. The B-band stretch is chosen to bring out the faintest possible outskirts of the galaxy; that for R-band is chosen to reveal more of the central details.
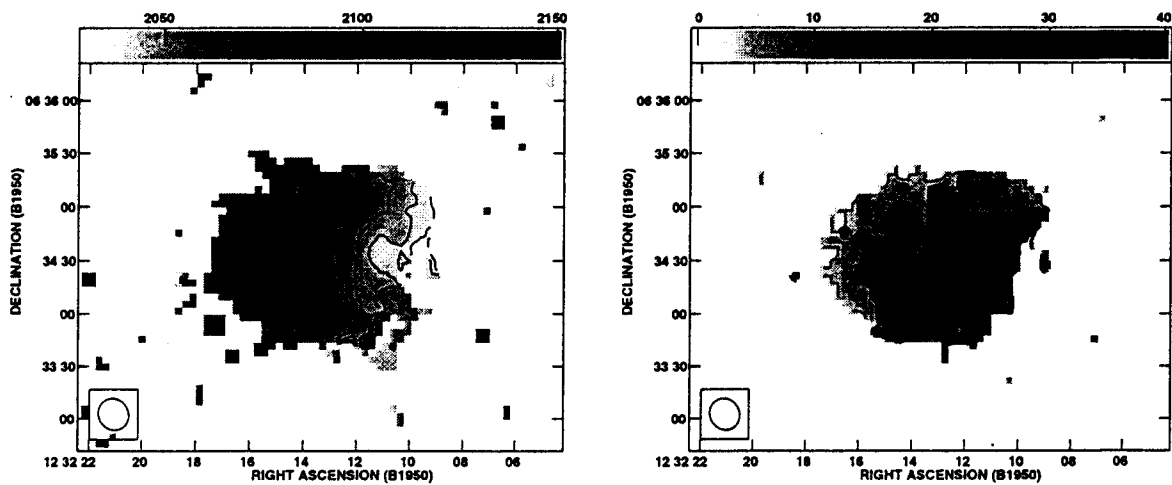
Fig. 10.— Isovelocity contours superimposed on a greyscale image of the velocity field (*left* panel) and of the second moment map (*right*) from the merged C+D data of DDO 137. Contours are drawn from 2030 to 2090 in steps of 10 km s^{-1} in the left-hand panel and from 5 to 20 in steps of 5 km s^{-1} in the right-hand one.

Fig. 11.— Rotation curve for DDO 137, determined by fitting the velocity field within consecutive annuli. The center position, systemic velocity (2060 km s^{-1}), and inclination were held fixed for all rings at values discussed in the text; the position angle was determined by the fit. Positive velocities are receding and positive radii are toward the E.
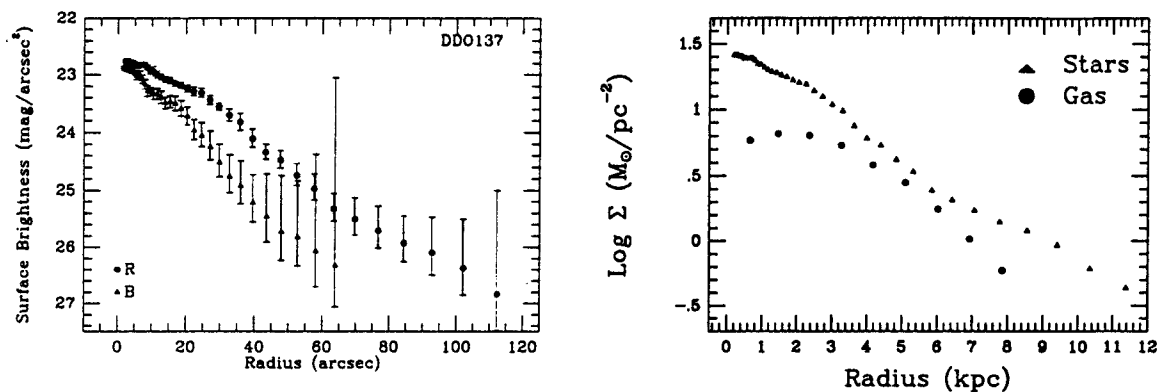
Fig. 12.— (*left panel*) B (*triangles*) and R (*circles*) surface brightness profiles for DDO 137 from Palomar CCD imaging. (*right panel*) Mass surface densities in stars (*triangles*) and gas (*circles*). We have assumed $M/L_R = 1 M_\odot/L_\odot$ for the purposes of this plot, and have included neutral hydrogen and primordial helium gas but have neglected molecular and ionized gas.
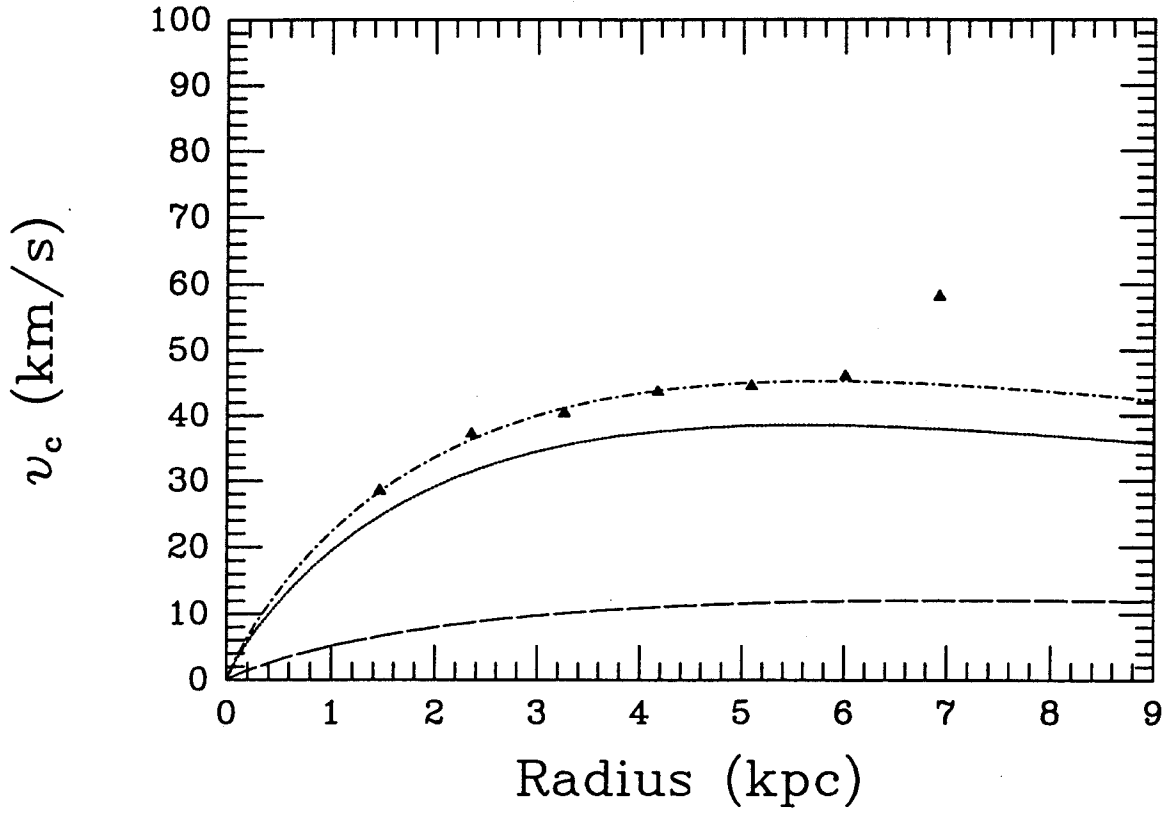
Fig. 13.— The rotation curve of DDO 137 (*points*) averaged over entire rings, with curves showing the contributions of exponential disks fitted to the stars assuming M/L_R = $1.8 M_\odot / L_\odot$ (*dotted*), to the gas, including neutral hydrogen and primordial helium (*dashed*), and to the sum of stars plus gas (*dash-dot*). This choice of mass-to-light ratio is close to the maximum disk value.
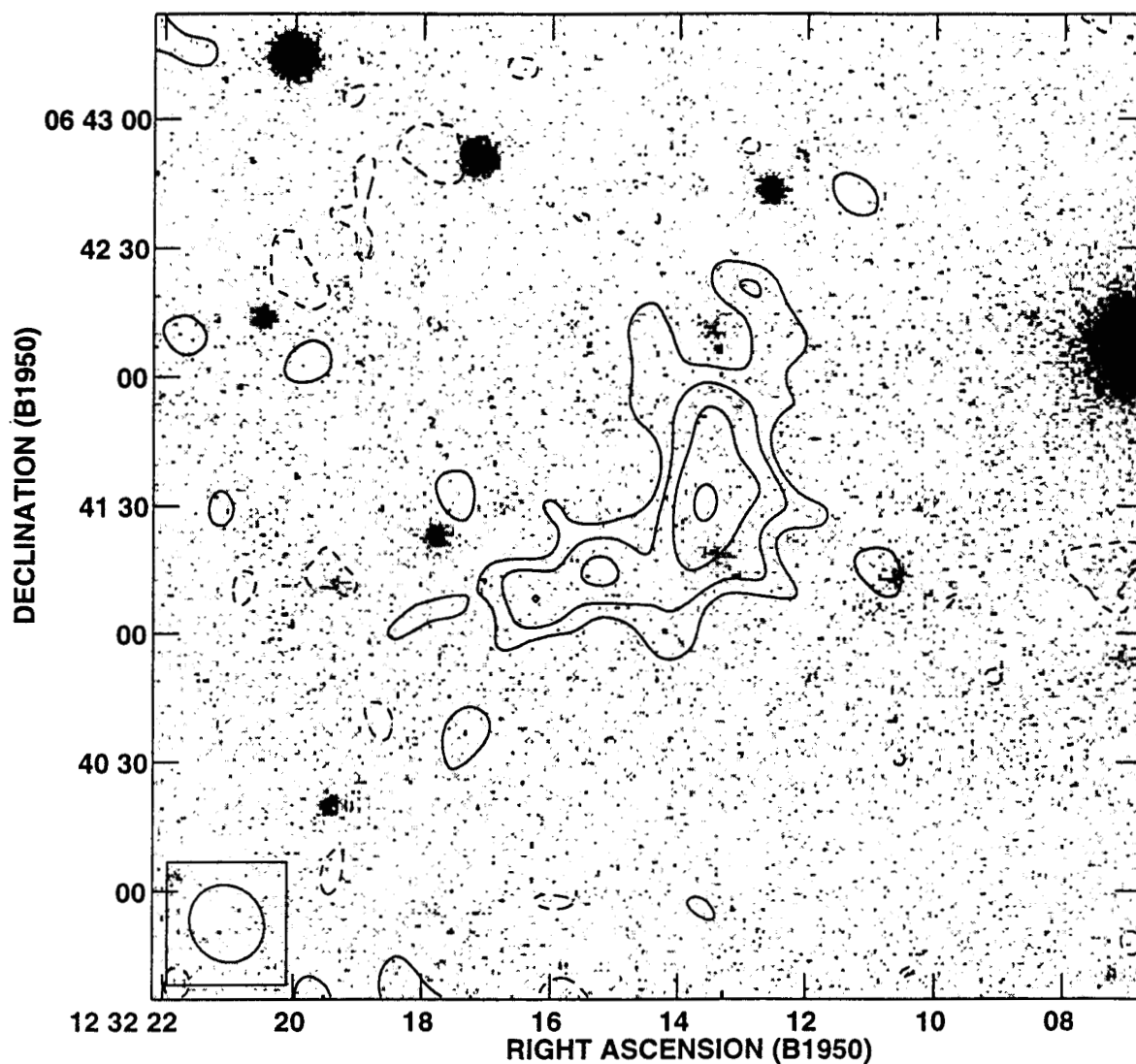
Fig. 14.— Contours of total hydrogen emission from Cloud A, integrated over all line-bearing channels from our C+D array combination. The contours are overlaid on a greyscale image of a B-band CCD frame from Lu (1997). Contour levels are −1.8, 1.8, 2.7, 4.0 and 6.1×10^{20} atoms cm^{-2}. The stretch in the B-band image is chosen to bring out the faintest possible features.

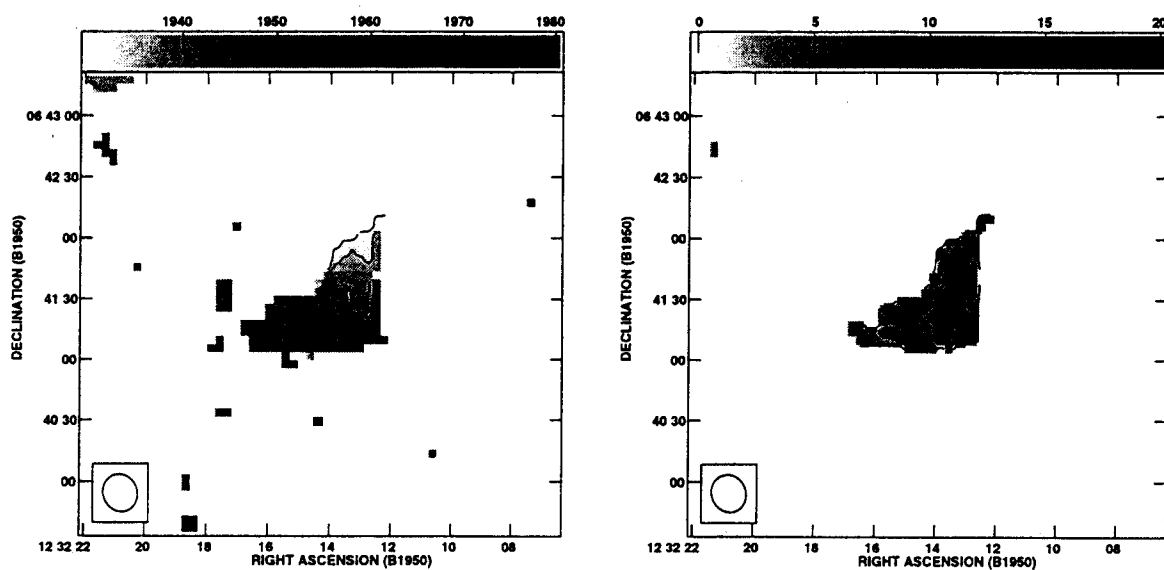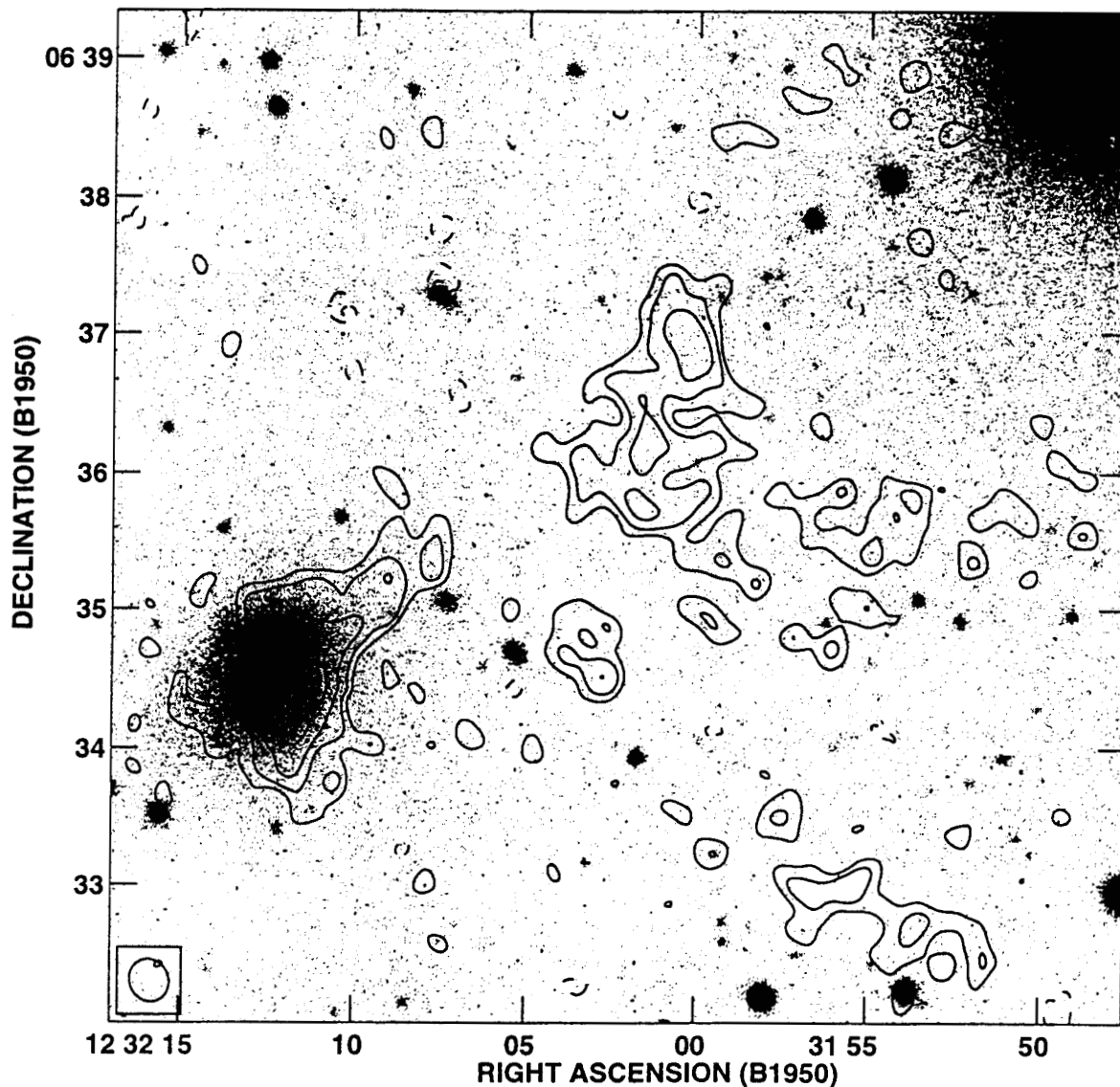Fig. 15.— Isovelocity contours superimposed on a greyscale image of the velocity field (*left*) and of the second moment map (*right*) of Cloud A from our combined C+D array data cube. Contours are drawn from 1930 to 1955 in steps of 5 $km\,s^{-1}$ in the left-hand panel and from 2 to 10 in steps of 4 $km\,s^{-1}$ in right-hand one.

Fig. 16.— Contours of total hydrogen emission from Cloud B, integrated over all line-bearing channels from our C+D array combination, overlaid on a greyscale image from the B-band CCD frame of Lu et al. (1998). Contour levels are -2.7, 2.7, 4.0, 6.1, 9.1, 13.6, 20.4, 30.6 and 45.9×10^{20} atoms cm^{-2}. Traces of DDO 137 remain near the left-hand edge of the frame. The B-band stretch is chosen to bring out the faintest possible features.
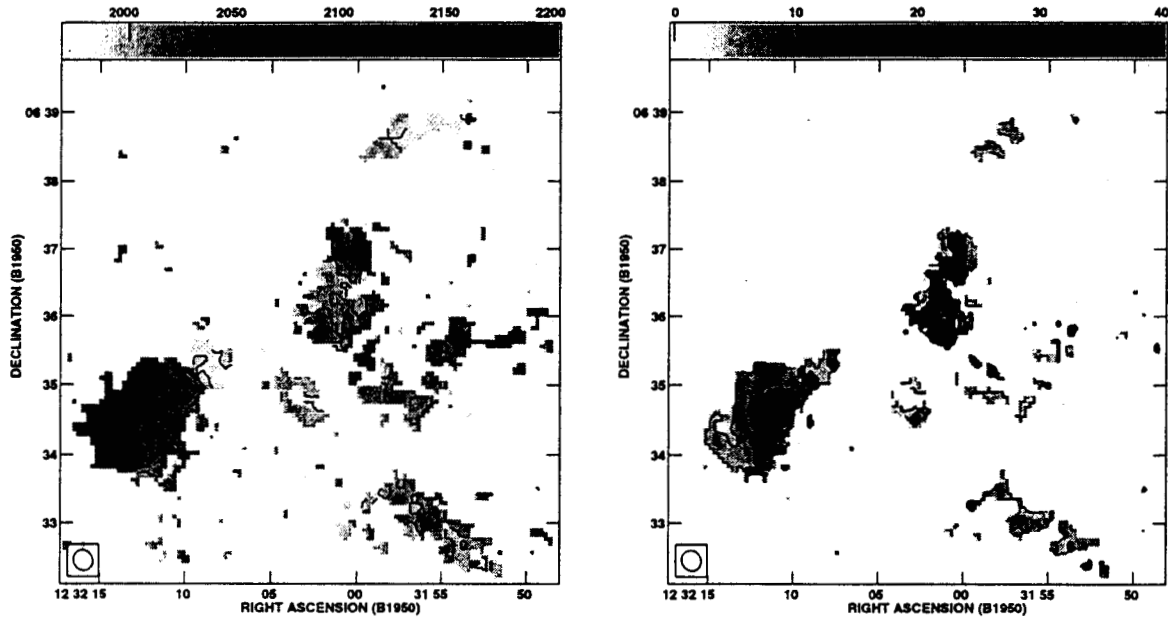
Fig. 17.— Isovelocity contours superimposed on a greyscale image of the velocity field (*left* panel) and of the second moment map (*right* panel) of Cloud B from our combined C+D array data cube. Contours are drawn from 1970 to 2070 in steps of 20 $km\,s^{-1}$ in the left-hand panel and from 5 to 25 in steps of 5 $km\,s^{-1}$ in the right-hand panel. Traces of DDO 137 are visible at the extreme E of each plot.
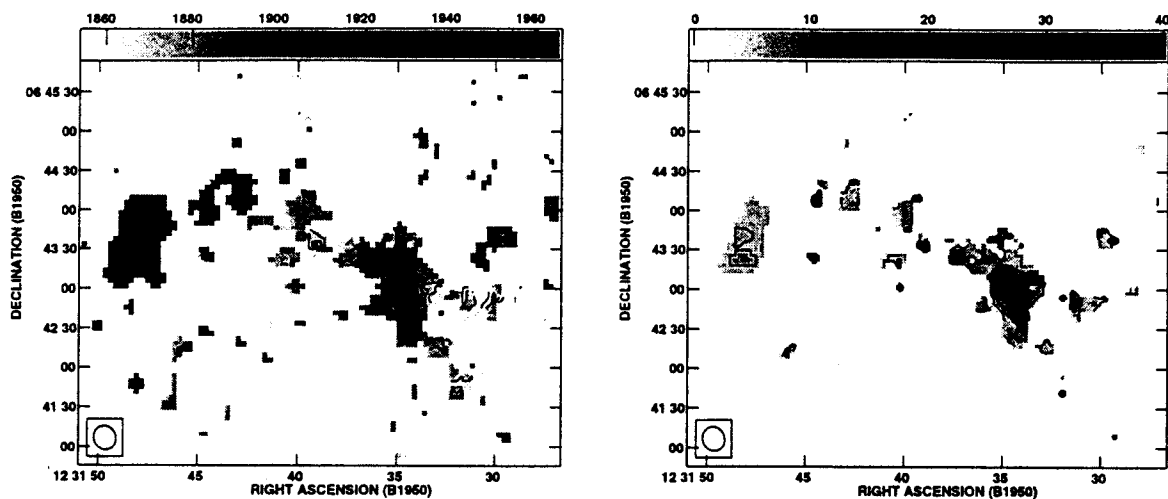
Fig. 18.— Contours of total hydrogen emission from Cloud C, integrated over all line-bearing channels from our C+D array combination. The contours are overlaid on a greyscale image from the B-band CCD frame of Lu et al. (1998). Contour levels are -2.5, 2.5, 3.8 and 5.6×10^{20} atoms cm^{-2}. Some traces of NGC 4532 are visible near the left edge of the figure. The B-band stretch emphasizes faint features. The "paper-clip" artifact just S of NGC 4532 is spurious.

Fig. 19.— Isovelocity contours superimposed on a greyscale image of the velocity field (*left*) and of the second moment map (*right*) of Cloud C from our C+D array data cube. Contours are drawn from 1855 to 1925 in steps of 10 km s^{-1} in the left-hand panel and from 5 to 20 in steps of 5 km s^{-1} in the right-hand panel. Traces of NGC 4532 are visible at the E edge of each plot.
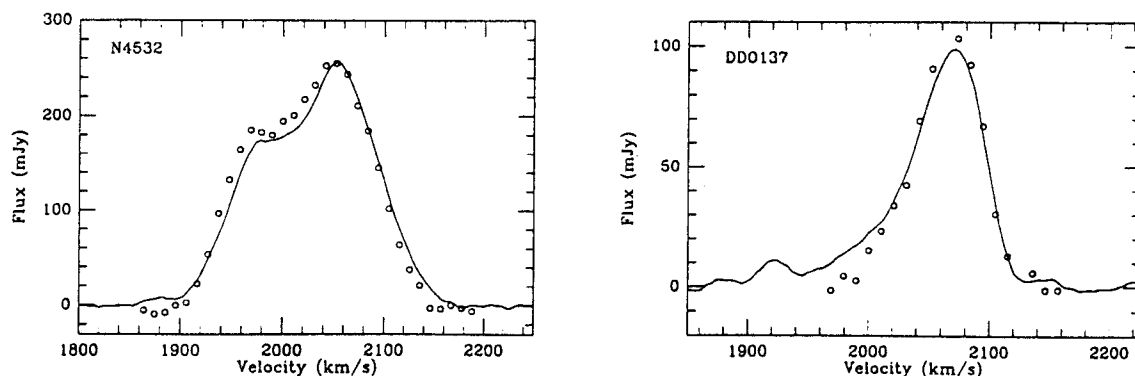

Fig. 20.— Spectra integrated over the individual galaxies (*open circles*) compared to the Arecibo central beam profile (*solid line*) for NGC 4532 (*left*) and DDO 137 (*right*).
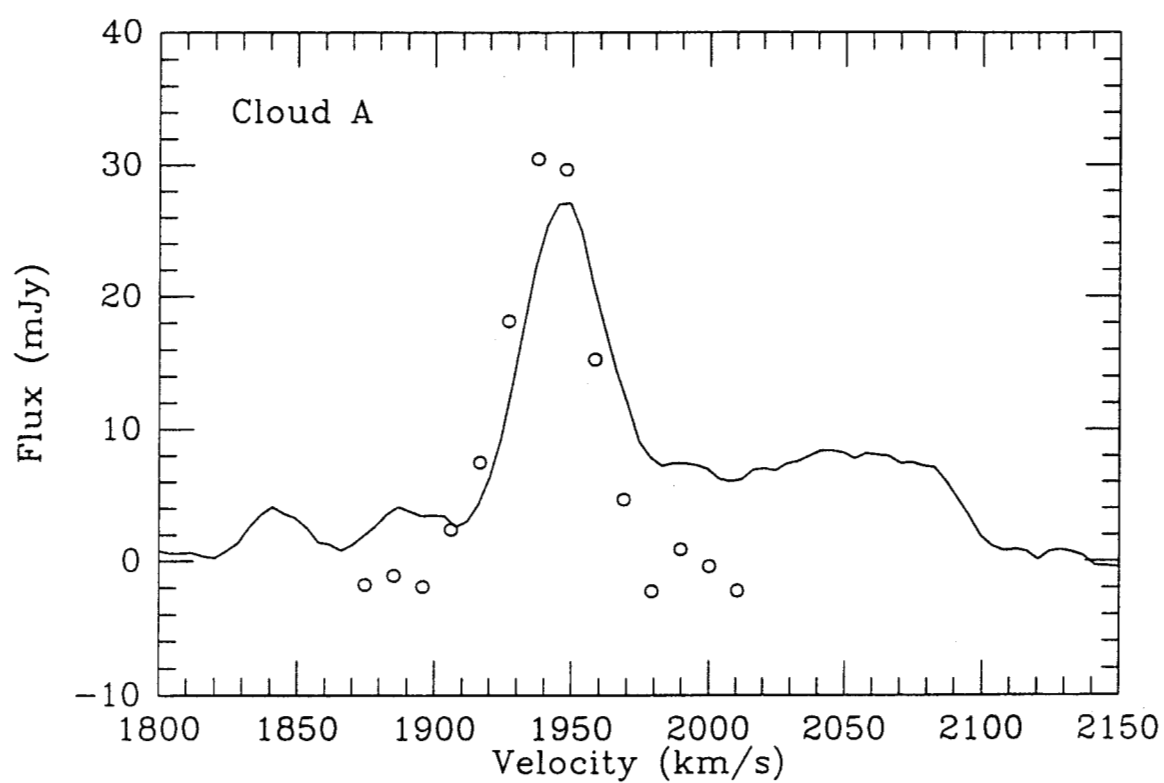
Fig. 21.— Spectrum integrated over Cloud A (*open circles*) compared to the Arecibo single beam profile (*solid line*) from the beam position closest to the cloud.
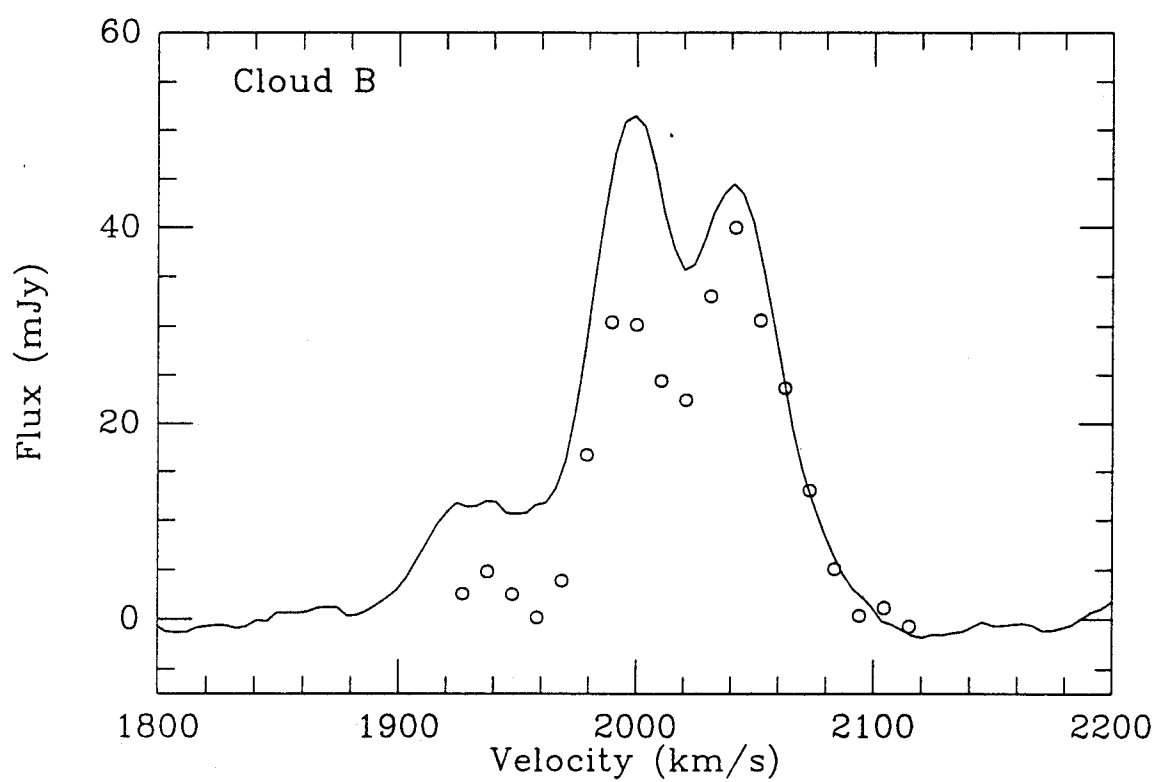
Fig. 22.— Spectrum integrated over Cloud B (*open circles*) compared to the Arecibo single beam profile (*solid line*) from the beam position closest to the cloud.
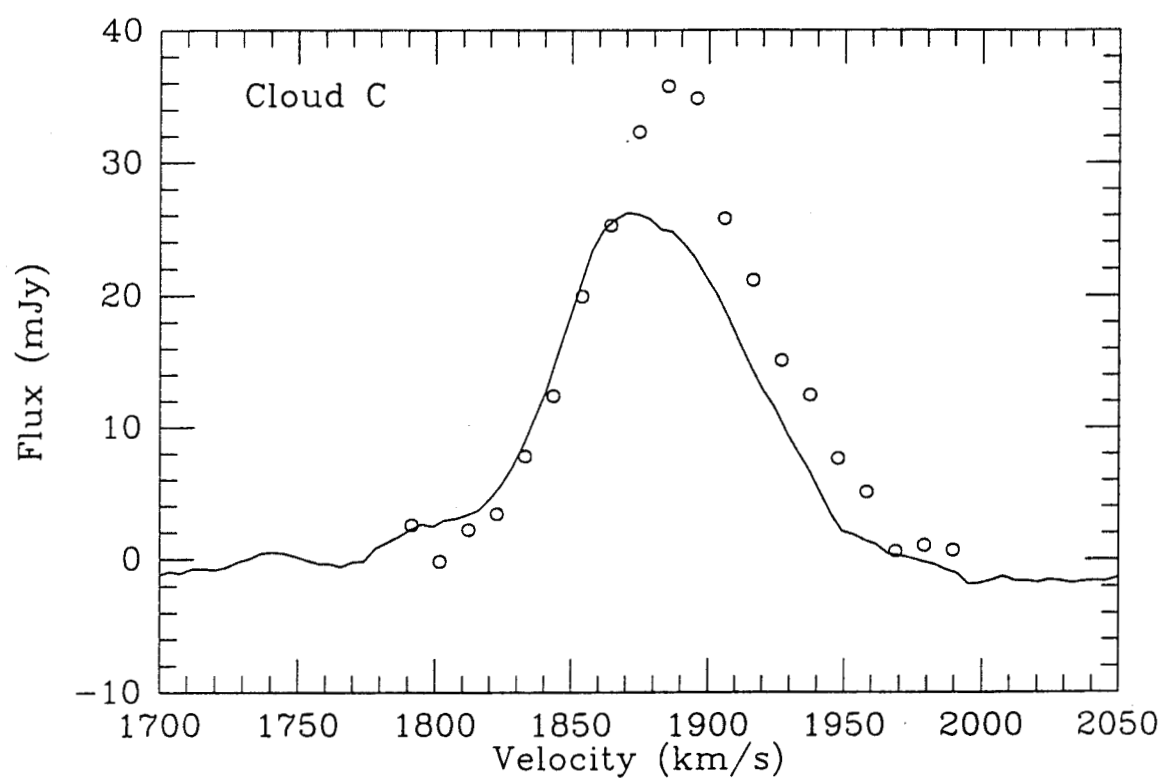
Fig. 23.— Spectrum integrated over Cloud C (*open circles*) compared to the Arecibo single beam profile (*solid line*) from the beam position closest to the cloud.